THE JOURNAL OF BIOLOGICAL CHEMISTRY VOL. 289, NO. 9, pp. 5371–5385, February 28, 2014

Cytosolic Dynamics of Annexin A6 Trigger Feedback Regulation of Hypertrophy via Atrial Natriuretic Peptide in Cardiomyocytes*[S]

Received for publication, August 29, 2013, and in revised form, January 7, 2014 Published, JBC Papers in Press, January 8, 2014, DOI 10.1074/jbc.M113.514810

Priyam Banerjee[1] **and Arun Bandyopadhyay**[2]

From the Cell Biology and Physiology Division, Council of Scientific and Industrial Research-Indian Institute of Chemical Biology, 4 Raja S. C. Mullick Road, Kolkata-700 032, West Bengal, India

Background: Altered annexin A6 expression is associated with several cardiovascular disorders, including myocyte hypertrophy, but precise functions of the protein remain elusive.
Results: Dynamic association of annexin A6 with intracellular atrial natriuretic peptide precursor protects against adrenergic stimulation-induced hypertrophy of H9c2 cardiomyocytes.
Conclusion: Annexin A6 negatively regulates hypertrophic progression of cardiomyocytes.
Significance: Annexin A6 exhibits potential for antihypertrophic therapeutics.

Malfunctions in regulatory pathways that control cell size are prominent in pathological cardiac hypertrophy. Here, we show annexin A6 (Anxa6) to be a crucial regulator of atrial natriuretic peptide (ANP)-mediated counterhypertrophic responses in cardiomyocytes. Adrenergic stimulation of H9c2 cardiomyocytes by phenylephrine (PE) increased the cell size with enhanced expression of biochemical markers of hypertrophy, concomitant with elevated expression and subcellular redistribution of Anxa6. Stable cell lines with controlled increase in Anxa6 levels were protected against PE-induced adverse changes, whereas Anxa6 knockdown augmented the hypertrophic responses. Strikingly, Anxa6 knockdown also abrogated PE-induced juxtanuclear accumulation of secretory granules (SG) containing ANP propeptides (pro-ANP), a signature of maladaptive hypertrophy having counteractive functions. Mechanistically, PE treatment prompted a dynamic association of Anxa6 with pro-ANP-SG, parallel to their participation in anterograde traffic, in an isoform-specific fashion. Moreover, Anxa6 mutants that failed to associate with pro-ANP hindered ANP-mediated protection against hypertrophy, which was rescued, at least partially, by WT Anxa6. Additionally, elevated intracellular calcium (Ca^{2+}) stimulated Anxa6-pro-ANP colocalization and membrane association. It also rescued pro-ANP translocation in cells expressing an Anxa6 mutant ($Anxa6^{\Delta C}$). Furthermore, stable overexpression of $Anxa6^{T356D}$, a mutant with superior flexibility, provided enhanced protection against PE, compared with WT, presumably due to enhanced membrane-binding capacity. Together, the present study delivers a cooperative mechanism where Anxa6 potentiates ANP-dependent counterhypertrophic responses in cardiomyocytes by facilitating regulated traffic of pro-ANP.

Mechanisms regulating cell size in metazoans remain poorly understood. In actively dividing cells, a balance between increase in cell number (hyperplasia) and size (hypertrophy) is instrumental for systemic homeostasis (1). However, in terminally differentiated cells, like cardiomyocytes of postnatal myocardium, regulation of hypertrophic process becomes crucial (2). Hypertrophy in cardiomyocytes occurs as a physiological phenomenon, as well as an adaptive response to stress, which may turn maladaptive. Pathological hypertrophy is a major risk factor in several cardiovascular disorders that culminate in heart failure (3). Understanding the molecular mechanisms of hypertrophic signaling and development of strategies to check hypertrophic growth remains a challenging quest in the cardiovascular arena of cell biology (4).

Anxa6,[3] largest member of the annexin family of Ca^{2+}- and phospholipid-binding proteins, is a major myocardial annexin (5). It is ubiquitously expressed and associated with a variety of physiological functions. Anxa6 predominantly serves as a scaffold protein for linking mediators of signaling pathways (6), preferably in a Ca^{2+}-dependent and membrane-proximal manner (7), which includes sarcolemma (8) as well as intracellular membranous structures (9–11). Functional redundancies arising from the highly conserved nature of annexins (12) remain a major reason for the lack of overt phenotypes in Anxa6 knockout animal models (13), where loss of Anxa6 function is believed to be mitigated by compensatory responses (14). However, it is known that end stage heart failure is associated with down-regulated Anxa6 (15), and the protein is unchanged to lowered in transition from hypertrophy to heart failure.

* This study was supported by Council of Scientific and Industrial Research (CSIR), Government of India, Grant BSC 0206 (to A. B.).
[S] This article contains supplemental Movies 1–7.
[1] Supported by a predoctoral research fellowship from CSIR.
[2] To whom correspondence should be addressed. Tel.: 91-033-2499-5791; Fax: 91-033-2473-5197; E-mail: arunb@iicb.res.in.

[3] The abbreviations used are: Anxa6, annexin A6; AFM, atomic force microscope; ANP, atrial natriuretic peptide; BAPTA-AM, 1,2-bis(2-aminophenoxy) ethane-*N*,*N*,*N*′,*N*′-tetraacetic acid tetrakis (acetoxymethyl ester); IP, immunoprecipitation; FL, full-length; MβCD, methyl-β-cyclodextrin; NLS, nuclear localization signal; Nppa, natriuretic peptide precursor A; PE, phenylephrine; pro-ANP, propeptide of atrial natriuretic peptide/intracellular precursor of atrial natriuretic peptide; qRT-PCR, quantitative real-time RT-PCR; SG, secretory granule(s); α-SkA, α-skeletal actin; WCL, whole cell lysate; LUT, lookup table; Iso, isoproterenol; EGFP, enhanced green fluorescence protein; WCL, whole cell lysate(s).

Onsets of cardiovascular pathological conditions are usually associated with an up-regulation of Anxa6 (16). We have characterized earlier a role of Anxa6 in the regulation of cardiomyocyte contractility (17). Moreover, Anxa6 is also considered to be a negative inotropic factor playing compensatory roles in chronic pathology (18). However, the mechanistic significance of altered Anxa6 expression in hypertrophied cardiomyocytes remains elusive.

In the present study, we investigated whether differential expression and spatiotemporal dynamics of Anxa6 are critically involved in the hypertrophic process of cardiomyocytes. For this purpose, a mechano-deficient cardiomyocyte cell line has been chosen. This line, H9c2(2-1), derived from rat heart, has been extensively characterized (19) and is an established animal origin-free model for studying signal transduction pathways in cardiomyocytes, including hypertrophy (20). Recently, it has also been shown that H9c2 and neonatal cardiomyocytes display identical hypertrophic responses (21), thus rendering the cells ideal for screening of antihypertrophic therapeutics.

Adrenergic stimulation of cardiomyocytes is a major contributor for triggering prohypertrophic cascades *in vivo* (22). Phenotypes in pathological hypertrophy are usually associated with changes in the gene expression or cytosolic distribution pattern of certain biochemical markers, predominantly the natriuretic peptides atrial natriuretic peptide (ANP) and brain natriuretic peptide and cytoskeletal proteins like α-SkA (α-skeletal actin). These constitute part of what is known as hypertrophy-associated "fetal gene reprogramming," a signature of the maladaptive pathology (4). ANP has also been shown to possess vital autocrine and paracrine functions locally, including antihypertrophic activities (23). Here we show that spatiotemporal alterations in Anxa6 expression are associated with PE-induced hypertrophic changes of H9c2 cardiomyocytes. Using stable cell lines of H9c2 cardiomyocytes, we found that Anxa6 confers substantial protection against hypertrophy through its association with pro-ANP, which is crucial for ANP-dependent protection against hypertrophy, acting ensemble as a negative feedback loop. Thus, the present study identifies a novel mechanistic spectrum of Anxa6 facilitating ANP-dependent counterhypertrophic cascades.

EXPERIMENTAL PROCEDURES

Reagents—Cell culture, molecular biology, and common laboratory reagents were procured from Invitrogen, Thermo Scientific (Waltham, MA), and Sigma, respectively, unless stated otherwise. Expression vectors were from Clontech, and shRNA plasmids from OriGene (Rockville, MD). PE, isoproterenol (Iso), and methyl-β-cyclodextrin (MβCD) were from Sigma. Ionomycin, BAPTA-AM, Alexa Fluor-tagged antibodies, fluorescent probe, and other microscopy consumables were from Molecular Probes, Inc. (Eugene, OR). Co-IP, Mem-PER, and subcellular fractionation kits were from Pierce. Primary antibodies were acquired from the following sources: Anxa6 (monoclonal) from BD Transduction Laboratories (Lexington, KY); Anxa6 (polyclonal), annexin A4, and α-SkA from Santa Cruz Biotechnology, Inc.; integrin-α4, α-tubulin, and GAPDH from Cell Signaling Technology (Beverly, MA); pro-ANP from Abcam (Cambridge, MA); ANP from Pierce; Living Colors antibody (JL-8) from Clontech; and pan-actin from Chemicon (Temecula, CA).

TABLE 1
List of oligonucleotides used for molecular cloning and site-directed mutagenesis

Name of oligos	Forward (5'→3')	Reverse (5'→3')
Anxa6-EGFPN1 / Anxa6-ZsYellow1N1	CCCAAGCTTATGGCCAAAATAGCAC ‡	AACTGCAGGTAGTCTTCTCCACCACAG
AcGFP1-Anxa6	CCCAAGCTTGGATGGCCAAAATAG	TGCACTGCAGTCGTCTTCTCCACC
SV40 3X NLS oligo	ACGCGTCGACGGATCCAAAAAAGAAGAGAAAGGTAGATCCAAAAAAGAAGAGAAAGGTAGATCCAAAAAAGAAGAGAAAGGTATCCCCGCGGGGA ‡‡	
Dendra2	ACCGGTCGCCACCATGAACACCCCGGG	ATGCGGCCGCTTACCACACCTGGCTGGG
Anxa6ΔN	CCCAAGCTTATGGGCACTGATGAGAAGTGC	AACTGCAGGTAGTCTTCTCCACCACAG
Anxa6ΔN1	AGGATGCCGAGGCTATGAGGCCGCTTGC	GCAAGCGGCCTCATAGCCTCGGCATCCT
Anxa6T356D	CGAGTCGAGCTGAAGGGTGACGTGCGTGCG	CGCACGCACGTCACCCTTCAGCTCGACTCG
Anxa6ΔNES	GACCTGAAGTCCGAGATGATGCCACCTGCC	GGCAGGTGGCATCATCTCGGACTTCAGGTC
Anxa6ΔVAAEIL	CTCAGGAAGATGCTCAGGAAATAGCAGACACACC	GGTGTGTCTGCTATTTCCTGAGCATCTTCCTGAG
Anxa6ΔC	CCCAAGCTTATGGCCAAAATAGCAC	GCGCAACTGCAGTGTCTCCACTGGGTGTGTC
proANP-EGFPN1	CCAAGCTTGGGATGGGCTCCTTC	CGGGATCCCATCTTCGGTACCG

‡ Boldface underline denotes restriction sites.
‡‡ Dashed/dotted underlines denote NLS repeats.

Molecular Cloning and Mutagenesis—Oligonucleotides used for cloning and mutagenesis are listed in Table 1. GFP- or YFP-tagged plasmid vectors expressing rat Anxa6 or pro-ANP were generated by standard molecular biology procedures. Dendra2-tagged plasmid was constructed by PCR-amplifying Dendra2 from Addgene (Cambridge, MA) plasmid 29574:tol2-mpx-Dendra2 (24) and swapping with EGFP in pEGFP-N1. The $Anxa6^{NLS}$ mutant was generated by ligating indicated nuclear localization signal (NLS) as a C-terminal fusion of Anxa6 in the AcGFP1-Anxa6 construct, without intervening stop codons. Site-directed mutagenesis was performed using the QuikChange Lightning kit (Stratagene, La Jolla, CA), following the manufacturer's instructions. Schematic maps of Anxa6 constructs are depicted in Figs. 3*A* and 6*A*. The pro-ANP-EGFP construct has been described elsewhere (25). Constructs were verified by automated sequencing at Eurofins Genomics (Bangalore, Karnataka, India).

Cell Culture, Transfection, Stable Cell Line Generation, and Treatments—The rat cardiomyocyte cell line H9c2(2-1), acquired from the cell repository of the National Centre for Cell Science (Ganeshkhind, Pune, India), was maintained in DMEM supplemented with 4.5 g/liter glucose, 1.5 g/liter sodium bicarbonate, 10% FBS, and antibiotics at 37 °C in a humidified atmosphere containing 5% CO_2. Before experimentation, cells were cultured in serum- and antibiotic-free growth medium for 24 h. For transient expression, 1–2 × 10^5 cells, seeded in 35-mm dishes, were transfected with 2–6 μg of plasmid DNA and 2–8 μl of FuGENE HD (Roche Applied Science) reagent, as per the manufacturer's instructions. Downstream experiments were performed after 72–96 h (knockdown experiments) or 48 h (all others) post-transfection. Adding selection antibiotics to transfected cells, according to predetermined kill curves, generated

TABLE 2
List of primers used for real-time PCR and RT-PCR

Name of primer	Forward (5′ → 3′)	Reverse (5′ → 3′)
Anxa6	GCCGCTTGCCTATTGTGAC	GCTGGTGTATCTGCTCATTGG
Anxa6.1/Anxa6.2	TGGCCACAGGAAATCGAGAGGAAG	GGTCATGAAGCGTGTCTCCAAGGAAG
Nppa	TCCTCTTCCTGGCCTTTTGGC	AGACGGGTTGCTTCCCCAGTC
α-SkA	TGAAGCCTCACTTCCTACCC	CGTCACACATGGTGTCTAGTTC
18 S rRNA	CGGCTACCACATCCAAGGAA	AGCTGGAATTACCGCGGC

stable clones. Primary selections were continued for 3 weeks, when clones with desired expression levels were aseptically transferred to 96-well plates and allowed to grow further in selection medium for 2 weeks before proceeding to experimentation. For induction of hypertrophy, cells were treated with 100 μM PE for 24 h (26), unless stated otherwise, and 10 μM Iso for 48 h (27). For Ca^{2+} and cholesterol perturbation experiments, cells were preincubated with 4 μM ionomycin for 10 min, with 10 μM BAPTA-AM for 30 min, or with 50 mM MβCD for 30 min.

Real-time Quantitative RT-PCR (qRT-PCR)—Primers used for qRT-PCR are listed in Table 2. Relative quantification of transcript profiles was performed as described earlier (28). Briefly, cDNA synthesized from 500 ng of total RNA extracted from cells, were subjected to quantitative PCR using SYBR Green chemistry. Computation of -fold changes in mRNA levels from C_T values using $2^{-\Delta\Delta CT}$ methods have been described elsewhere (29). 18 S rRNA levels were used as an internal reference standard.

Subcellular Fractionation, Co-IP, and Western Immunoblotting—Whole cell lysates (WCL) were prepared in CellLytic MT lysis buffer (Sigma) supplemented with Halt protease and phosphatase inhibitor mixture (Pierce). Subcellular fractionation, membrane protein extraction using a Mem-PER kit, and co-IP were carried out as per the manufacturer's instructions. For co-IP, about 1 mg of lysate was subjected to IP, and 10% of the starting material was taken as input. Lysates were incubated with antibody-coupled or control resins overnight at 4 °C with end-on rotation. 25–100 μg of elutes were used for subsequent Western blot analysis. SDS-PAGE, immunoblotting, detection, and densitometric quantification were performed as described elsewhere (28).

Enzyme-linked Immunosorbent Assay (ELISA)—The levels of ANP in the cell culture medium were measured by a double-antibody sandwich ELISA, using a commercially available kit from Qayee-Bio (Shanghai, China) according to the manufacturer's instructions. Briefly, culture media from control and treated cells were collected and centrifuged at 3000 rpm for 20 min, and the supernatant was incubated with HRP conjugates in antibody-coated wells of microwell plates. Signal detection was carried out in a Spectramax Paradigm multimode detection platform (Molecular Devices, Sunnyvale, CA).

Microscopy—Confocal imaging was performed primarily on a DMIRB microscope equipped with a TCS-SP2 confocal point scanner (Leica Microsystems, Mannheim, Germany), six laser lines (361-, 458-, 488-, 514-, 543-, and 633-nm HeNe), and three PMT detectors. ×63/1.32 numerical aperture or ×100/1.4 numerical aperture oil immersion objectives were used for image acquisition via Leica LCS software. For some live cell imaging experiments, a Revolution XD system (Andor Technology, Belfast, UK) equipped with an Olympus IX81 microscope, Yokogawa CSU-X1 spinning disc confocal unit, three laser lines (405, 488, and 561 nm), and iXon 897 EMCCD camera was used. A ×60/1.42 numerical aperture oil immersion objective was used for image acquisition via Andor iQ version 2.7 software.

High-resolution images were acquired sequentially with a slow unidirectional scanning speed (200–400 Hz; beam expander: 6), and smaller frame sizes were used for higher magnification. For time lapse imaging, faster scanning speeds (800–1000 Hz) coupled with low line averaging were used to preserve temporal resolution. Pixel dimensions and *Z*-steps were estimated to satisfy Nyquist sampling criteria. The disc spinning speed of the CSU unit was set to 1800 rpm. All comparable sets of images were acquired under identical stack parameters, laser power, detector gain, amplifier offset, and pinhole aperture windows.

Atomic force microscopy of live cells was carried out in CO_2-independent live cell imaging media (Molecular Probes) by Magnetic AC mode using an Agilent (La Jolla, CA) 5500-ILM AFM with a piezo-scanner (maximum range, 100 μm). Microfabricated Type-II Magnetic AC silicon cantilevers (Agilent) of 235-μm length and with a nominal spring force constant of 0.5–9.5 newtons/m were used. Cantilever oscillation frequency was tuned into resonance frequency of about 45–115 kHz. Images were captured at frame sizes of 512 × 512 pixels with a scanning speed of 0.5 lines/s.

Immunocytochemistry and Live Cell Imaging—Cells cultured in LabTek-II chambered coverglass (Nunc, Roskilde, Denmark) were fixed with 3.7% paraformaldehyde for 10 min, quenched in 50 mM NH_4Cl for 15 min, and permeabilized using 0.2% Triton X-100 for 5 min, followed by blocking with Image-iT FX signal enhancer (Molecular Probes) for 30 min and 1% BSA for 1 h at room temperature. F-actin staining was performed with Alexa Fluor 532 phalloidin as per the manufacturer's instructions. For immunofluorescence, primary antibody incubation was performed in 1% BSA for 2 h at room temperature or overnight at 4 °C, followed by incubation with Alexa Fluor-conjugated secondary antibodies (1:500) in 1% BSA for 1 h (room temperature). Nuclear counterstaining was performed with DAPI or TO-PRO-3. Cells were washed 3 times after each step with DPBS, which was also used as solvent in previous steps. Stained cells were kept under DPBS and imaged within 24 h.

For live cell imaging, cells cultured in 35-mm glass bottom dishes (MatTek, Ashland, MA) were imaged in CO_2-independent live cell imaging medium within a climate box mounted onstage. Dendra2 photoswitching was performed with little modification of previously described methods (30). Briefly, unconverted Dendra2 (green) was irreversibly photoswitched to its red form (supplemental Movie 2) by UV laser, for 500 ms,

which enabled simultaneous detection of EGFP signal in cotransfected cells without bleaching EGFP (data not shown). Unconverted and photoconverted forms were simultaneously tracked at 500–540 and 575–625 nm with 488- and 543-nm laser lines, respectively.

Image Processing—All images were processed with ImageJ (National Institutes of Health, Bethesda, MD) using identical linear adjustment parameters across comparable groups. Images were iteratively deconvolved for improving the signal/noise ratio. For quantification purposes where binary images were instrumental, an adaptive threshold algorithm was applied for dynamic segmentation. All time stacks were bleach-corrected using a histogram-matching macro. For measurement of hypertrophy, individual cell areas of thresholded 8-bit grayscale images were outlined with a tracing tool macro. Output area measurements were acquired from the masked outlines and expressed as -fold change in treated groups over control. Only cells whose areas lie completely within the field of view were considered. Colocalization analysis was performed with JACoP, as described elsewhere (31). Briefly, the percentage of colocalization was calculated from Manders' coefficients as the fraction of green channel overlapping red. In-built particle-tracking algorithms in ImageJ were used to measure vesicular structures in cytosol. Tracking of clusters in time lapse series were performed using the MTrackJ plugin, and data were plotted as described (32). Atomic force microscopy images were flattened using PicoView version 1.12 (Agilent) and assigned the indicated LUT using Pico Image advanced (Agilent).

Statistical Analysis—All experiments were repeated at least three times, and representative data are displayed. Statistics were performed using Prism 5 (GraphPad Software, La Jolla, CA). Unless stated otherwise, values represent mean ± S.E. Unpaired, two-tailed Student's t test was used to compare means, and $p < 0.05$ was considered statistically significant.

RESULTS

PE Induces Reversible Hypertrophic Transformation of H9c2 Cardiomyocytes—Treatment with 100 μM PE for 24 h resulted in increased volume over control as revealed by atomic force microscopy of live cells (Fig. 1*A*). Measurement of cell surface area by actin staining with fluorescent phalloidin (Fig. 1*B*) displayed a 2.2-fold increase in the area of PE-treated cells (Fig. 1*C*) and transformed relaxed actin filaments into a complex web of stress fibers (Fig. 1*D*) with prominent actin incorporation into the fibers (Fig. 1*E*). Analysis of relative transcript levels of hypertrophic markers Nppa and α-SkA by qRT-PCR (Fig. 1*F*) showed a 6-fold up-regulation for Nppa and 5-fold for α-SkA. Immunoblotting of WCL for ANP precursor, pro-ANP, and α-SkA (Fig. 1*G*) displayed a ~2.5-fold increase of either candidate by PE (Fig. 1*H*). It also increased perinuclear accumulation of secretory granules containing pro-ANP (Fig. 1*I*). Furthermore, PE-induced increases in cell surface area of H9c2 cells were found to be reversible (Fig. 1*J*), as shown by significant restoration of cell area after PE withdrawal (Fig. 1*K*).

Anxa6 Is Spatiotemporally Reorganized in the Course of Hypertrophic Progression—To assess the Anxa6 expression pattern in hypertrophied cells, relative mRNA levels of Anxa6 (Fig. 2*A*) were analyzed by qRT-PCR, which showed 3.5-fold increase. Immunoblot analysis on WCL (Fig. 2*B*) showed a progressive increase in Anxa6 protein levels by PE at the indicated time points (Fig. 2*C*), with significant increases at 12 and 24 h. Assessment of changes in intracellular distribution of Anxa6 by time lapse immunostaining (Fig. 2*D*) displayed an increase in the signal of Anxa6 across the time points (Fig. 2*D*, *insets*) that spread out from the nuclear periphery toward the membrane after 24 hours of PE treatment. Interestingly, Anxa6 displayed a punctate staining pattern in the juxtanuclear cytosol, the number and size of which, increased with duration of PE treatment (Fig. 2, *E* and *F*). A punctate appearance of Anxa6 has been reported earlier in some cell types (33, 34), where Anxa6 participated in membrane trafficking. To inquire whether such a punctate staining pattern of Anxa6 indicates its association with membranous structures, a subcellular fractionation followed by immunoblot analysis was performed. It showed that Anxa6 was associated mostly with membrane fractions, including the limiting membrane as well as the intracellular membranous entities (Fig. 2, *G* and *H*).

Controlled Up-regulation of Anxa6 Protects against PE-induced Hypertrophy—To gain functional insight into the differential expression and localization of Anxa6 between control and hypertrophied states, stable cell lines expressing Anxa6-YFP ($H9c2^{Anxa6\text{-}YFP}$) or empty vector ($H9c2^{YFP}$) were generated (Fig. 3*B*), with transfection and clonal selection titered to match Anxa6 protein levels observed in PE-treated cells (Figs. 2*A* and 3*C*). Such calibrations were instrumental, given that a 10-fold overexpression of Anxa6 targeted to the heart negatively affected cardiomyocyte function in transgenic mice (35). $H9c2^{Anxa6\text{-}YFP}$ cells displayed reduced nuclear signal of YFP and speckled signals from granular structures in juxtanuclear cytosol (Fig. 3*B*) that transformed into profuse clusters extending from the nuclear to cellular periphery upon PE treatment (supplemental Movies 1 and 5), similar to the ones observed in Fig. 2*D*. Surprisingly, AFM screening displayed grossly unaltered cellular volume following PE treatment of $H9c2^{Anxa6\text{-}YFP}$ cells (Fig. 3*D*), unlike that observed in Fig. 1*A*. To address whether the controlled up-regulation of Anxa6 prevented PE-induced hypertrophy, cellular morphometric analysis was carried out by phalloidin staining of $H9c2^{YFP}$ or $H9c2^{Anxa6\text{-}YFP}$ cells (Fig. 3*E*) at the indicated time points after PE addition. The $H9c2^{YFP}$ cells showed an increase in area similar to WT cells (Fig. 1*J*). In contrast, quantification of cell surface area (Fig. 3*F*) revealed that not only were the $H9c2^{Anxa6\text{-}YFP}$ cells significantly protected from the PE-induced increase in cell surface area, but also their rates of recovery during the withdrawal phase were significantly faster than those of $H9c2^{YFP}$ cells. Furthermore, transcript levels of Nppa and α-SkA were analyzed by qRT-PCR (Fig. 3*G*). In contrast to WT cells, which displayed ~6-fold higher transcript levels of the two markers (Fig. 1*F*) by PE, $H9c2^{Anxa6\text{-}YFP}$ cells showed 2.5-fold rise, indicating a truncated hypertrophic response. Thus, it is likely that Anxa6 confers a sustained (both under treatment and postwithdrawal) protection against PE-induced hypertrophy of cardiomyocytes.

Down-regulation of Anxa6 Augments Hypertrophy, albeit It Abrogates the Perinuclear Vesicular Architecture of Pro-ANP in Hypertrophied Cells—To assess whether Anxa6 is necessary for the endogenous regulatory mechanism to resist hypertrophy-

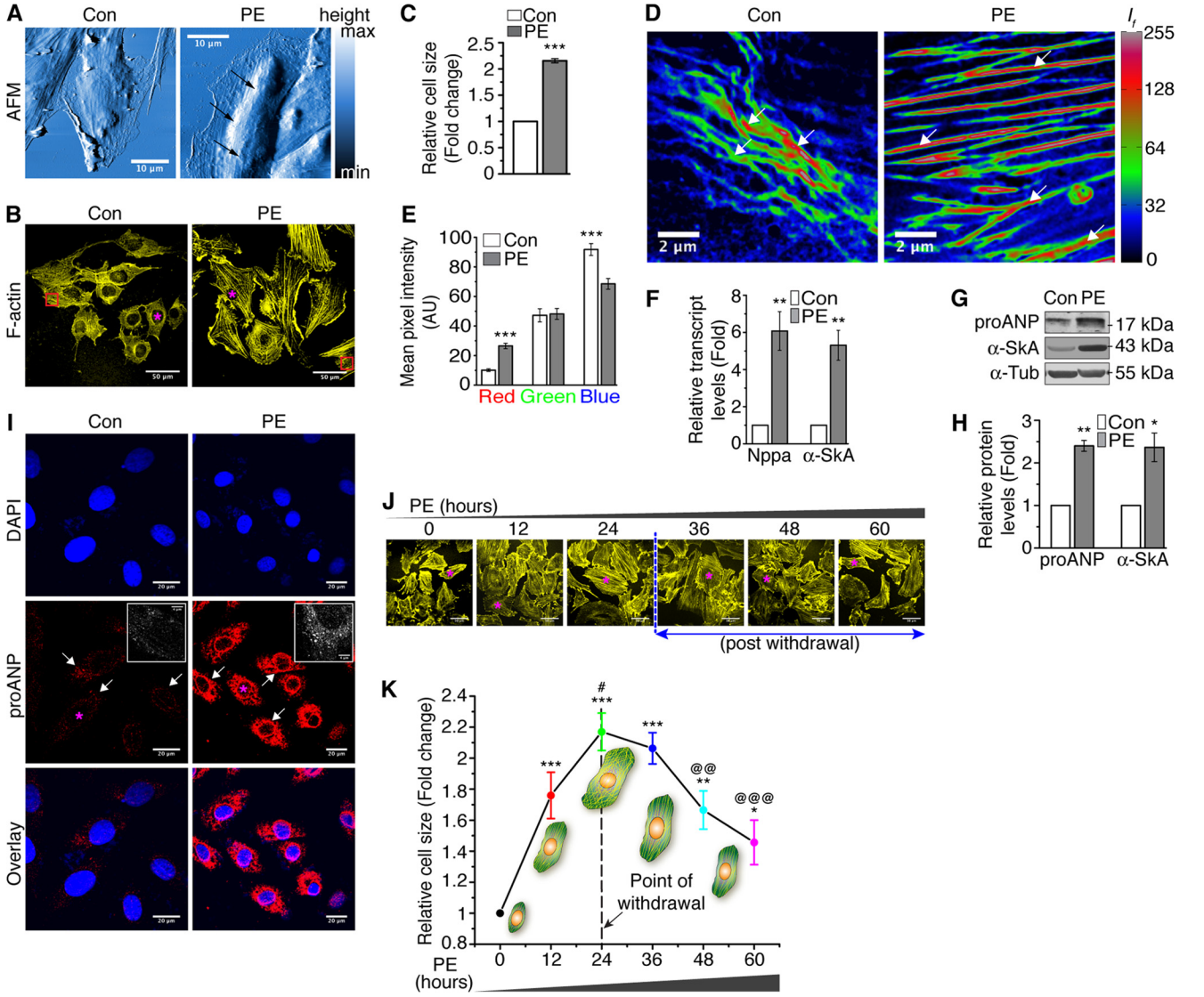

FIGURE 1. **Characterization of PE induced hypertrophy of H9c2 cardiomyocytes.** Cells treated with 100 μM PE for 24 h were analyzed for hypertrophy-associated changes. *A*, AFM images of live cells. The *LUT bar* corresponds to height. *Arrowheads*, maximum height. *Scale bar*, 10 μm. *B*, confocal micrographs of fixed cells stained with phalloidin for F-actin. *Scale bar*, 50 μm. *Red boxes* are shown *magnified* in *D*. A *magenta star* denotes typical representatives. *C*, -fold change in cell surface area after PE treatment; $n = 100$ cells; ***, $p < 0.0001$. *D*, confocal micrographs of relaxed *versus* stressed actin filaments (intensity *pseudocolored* as per the indicated LUT) from *red boxes* in *B*. *Arrowheads*, actin incorporation into fibers. *Scale bar*, 2 μm. *E*, quantification of pixel intensities from the indicated *color-coded landscapes* in *D*; means ± S.E. (*error bars*) of $n = 12$ fields per group; ***, $p < 0.0001$. *F*, -fold changes of Nppa and α-SkA mRNA levels in PE-treated cells, analyzed by qRT-PCR; $n = 3$; **, $p < 0.01$. *G*, immunoblot showing pro-ANP and α-SkA protein levels in WCL from control or PE-treated cells. α-Tubulin was used as loading control. *H*, -fold changes of pro-ANP and α-SkA protein levels in PE-treated cells, analyzed by densitometric quantification of G; $n = 3$; **, $p < 0.01$; *, $p < 0.05$. *I*, cells immunostained for pro-ANP. Nuclei were counterstained with DAPI. *Arrowheads*, perinuclear signal. *Scale bar*, 20 μm. *Insets*, juxtanuclear pro-ANP clusters. *Scale bar*, 4 μm. *J*, confocal images of H9c2 cells fixed at the indicated time points after PE addition and stained for F-actin with Alexa Fluor 532 phalloidin. *Scale bar*, 50 μm. The *magenta star* at the *center* of a cell denotes typical representatives of each group. *K*, plot of the increase in cell size across PE treatment for the indicated time periods and restoration of cell size after PE withdrawal. Cell area was measured by phalloidin staining; $n = 50$ cells; -fold changes over $t = 0$; *** and @@@, $p < 0.0001$; ** and @@, $p < 0.01$; * and #, $p < 0.05$ (*, $t = 0$; #, $t = 12$; @, $t = 24$). *Dotted line*, point of PE withdrawal.

associated changes, stable cell lines ($H9c2^{shR}$) expressing Anxa6 ($H9c2^{Anxa6shR}$) or scrambled ($H9c2^{ScrambshR}$) shRNA were generated (Fig. 4*A*). qRT-PCR and immunoblot analysis showed an 80% reduction in Anxa6 expression levels (Fig. 4, *B–D*). AFM analysis of live $H9c2^{Anxa6shR}$ cells showed a substantial increase in cell volume by PE, compared with control (Fig. 4*E*). Phalloidin staining (Fig. 4*F*) revealed a 15% additional increase in the area of $H9c2^{Anxa6shR}$ cells compared with $H9c2^{ScrambshR}$ (Fig. 4*G*). Surprisingly, immunocytochemistry showed unchanged to an insignificant accumulation of pro-ANP-SG (Fig. 4*H*) in $H9c2^{Anxa6shR}$ cells under PE treatment. $H9c2^{ScrambshR}$ showed juxtanuclear pro-ANP accumulation, similar to WT (Fig. 1*I*). Immunoblotting also displayed $H9c2^{ScrambshR}$ cells having significantly higher levels of pro-ANP and α-SkA upon PE treatment. However, pro-ANP levels were found to be unaltered in $H9c2^{Anxa6shR}$ cells treated with PE (Fig. 4, *I* and *J*). In contrast, the Nppa transcript level was 6-fold higher in both $H9c2^{ScrambshR}$ and $H9c2^{Anxa6shR}$ cells compared with control (Fig. 4*K*). Thus, it seems that a lack of Anxa6 in H9c2 cardiomyocytes aggravates hypertrophy but abrogates hypertrophy-associated accumulation of pro-ANP vesicles in cytosol, without affecting ANP gene expression.

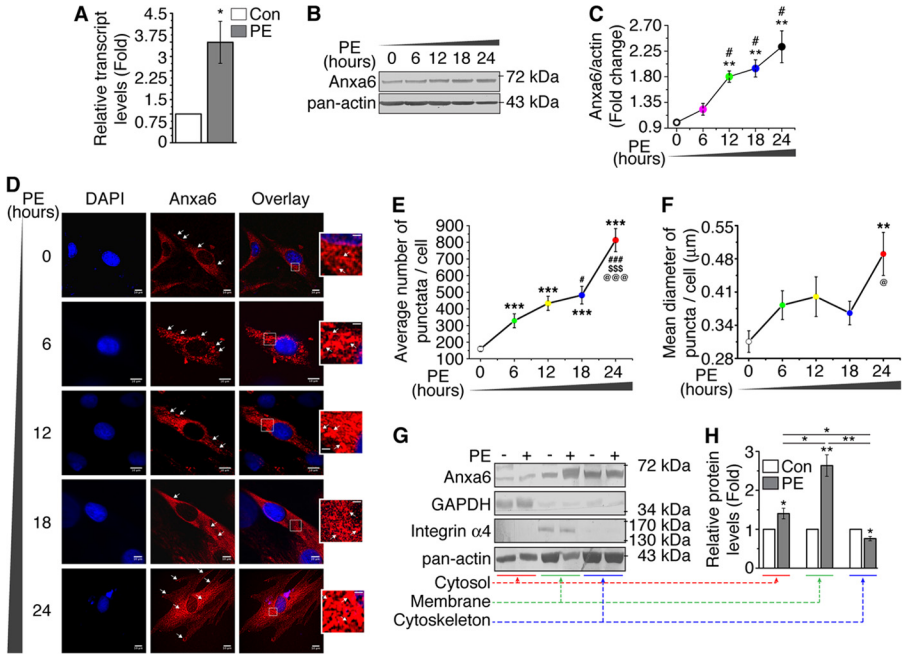

FIGURE 2. **Elevated expression profile accompanies a spatiotemporal redistribution of Anxa6 in the course of PE treatment.** H9c2 cells treated with PE for 24 h were analyzed for temporal and spatial alterations in Anxa6 levels. *A*, relative levels of Anxa6 mRNA in control and PE-treated cells ($t = 24$ h), quantified by qRT-PCR and presented as -fold change over control. Values are means ± S.E. (*error bars*) of $n = 3$ experiments; *, $p < 0.05$. *B*, immunoblot showing Anxa6 protein profile in WCL prepared at the indicated time points after PE addition. Pan-actin was used as a loading control. *C*, Anxa6 protein levels at the indicated time points after PE addition, analyzed by densitometric quantification of *B*. Shown is -fold change over $t = 0$, $n = 3$; **, p (with $t = 0$) < 0.01; #, p (with $t = 6$) < 0.01. *D*, analysis of changes in Anxa6 localization. Cells at the given time points after PE addition were immunostained for Anxa6 and analyzed by confocal microscopy. Nuclei were counterstained with DAPI. *Arrowheads*, punctate vesicular structures. *Scale bar*, 10 μm. *Insets*, magnified view of juxtanuclear cytosol showing the progressive appearance of puncta with increased expression levels. *Scale bar*, 2 μm. Plots showing relative number (*E*) and diameter (*F*) of Anxa6 punctate structures from thresholded images as shown in *D*. Shown are means ± S.E. of $n = 15$ cells; ***, ###, $$$, and @@@, $p < 0.0001$; **, $p < 0.01$; # and @, $p < 0.05$ (*, with $t = 0$; #, with $t = 6$; $, with $t = 12$; @, with $t = 18$). *G*, immunoblot of Anxa6 protein levels in subcellular fractions, without PE (−) or treated with PE (+). Pan-actin, integrin-α4, and GAPDH were used as loading controls for cytoskeletal, membrane, and cytosolic fractions, respectively. *H*, densitometric quantification of *G*, showing Anxa6 protein levels from the indicated fractions in control or PE-treated cells. -Fold changes in PE over control of respective fractions; $n = 3$; **, $p < 0.01$; *, $p < 0.05$.

Anxa6 Progressively Associates with Pro-ANP in the Course of PE Treatment—Negative modulation of pro-ANP in hypertrophied H9c2$^{\text{Anxa6shR}}$ cells raised the possibility of interaction of the two proteins or formation of a shared complex that can accommodate the load of cytosolic pro-ANP accumulation in hypertrophied cells. To address this question, colocalization analysis was performed on confocal images of WT cells, double-immunostained for Anxa6 and pro-ANP at the indicated time points after PE addition (Fig. 5*A*). As shown, Anxa6 increasingly colocalized with pro-ANP in course of PE treatment (Fig. 5*B*), where high magnification sections revealed an increase in colocalized cluster sizes in the course of PE treatment. To assess whether Anxa6 physically associates with pro-ANP or pro-ANP-SG, a co-IP experiment was performed with WT cells, without PE (−) or treated with PE (+) (Fig. 5*C*). pro-ANP was present in Anxa6 immunoprecipitate in both control and treated cells. Similarly, reverse IP showed the presence of Anxa6 in pro-ANP immunoprecipitate of either group, and the association was seemingly higher under PE-treated conditions, indicating a progressive order of association between the two candidates.

Anxa6 Dynamically Associates with Pro-ANP in Hypertrophied Cardiomyocytes and Participates in Anterograde Traffic—PE-induced changes in Anxa6 gene expression and the punctate nature of cytosolic distribution, together with its pattern of colocalization with pro-ANP, indicated a dynamic nature of Anxa6 in cytosol of the cells undergoing hypertrophic transformation. To examine the dynamic nature of Anxa6-pro-ANP association and its involvement in anterograde traffic, cells transiently cotransfected with plasmids encoding pro-ANP-EGFP and Anxa6-Dendra2 were treated with PE for 6 h (time point of appearance of Anxa6 puncta). Photoconversion of Dendra2 tagged with Anxa6 showed dynamic association of Anxa6 with pro-ANP vesicles (supplemental Movie 3), resulting in its punctate appearance. Tracking overlapped paths of pro-ANP-EGFP and Anxa6-Dendra2 raised the possibility of Anxa6 participating in anterograde vesicular transport of pro-ANP (data not shown). To visualize whether Anxa6 participates in such forward traffic, movement of a single Anxa6 cluster was tracked in H9c2$^{\text{Anxa6-YFP}}$ cells, 6 h post-PE treatment (supplemental Movie 4), and of multiple such clusters in H9c2$^{\text{Anxa6-EGFP}}$ cells, 24 h post-PE treatment (supplemental Movie 5). As shown, the cluster of Anxa6 scans the perinuclear region before adapting a linear path toward the plasma membrane (Fig. 5*D*).

Anxa6 Provides Protection against PE via ANP-dependent Counterhypertrophic Mechanisms—To evaluate whether antihypertrophic functions of Anxa6 depend upon pro-ANP-dependent mechanisms, we adopted a site-directed mutagenesis approach (Fig. 6*A*). As shown in Fig. 6, *B* and *C*, mutations disrupting the N-terminal (Anxa6$^{\Delta N}$) tail (residues 1–89) or first annexin (Anxa6$^{\Delta N1}$) repeat (residues 29–89) altered the cytosolic localization pattern of Anxa6 and completely abol-

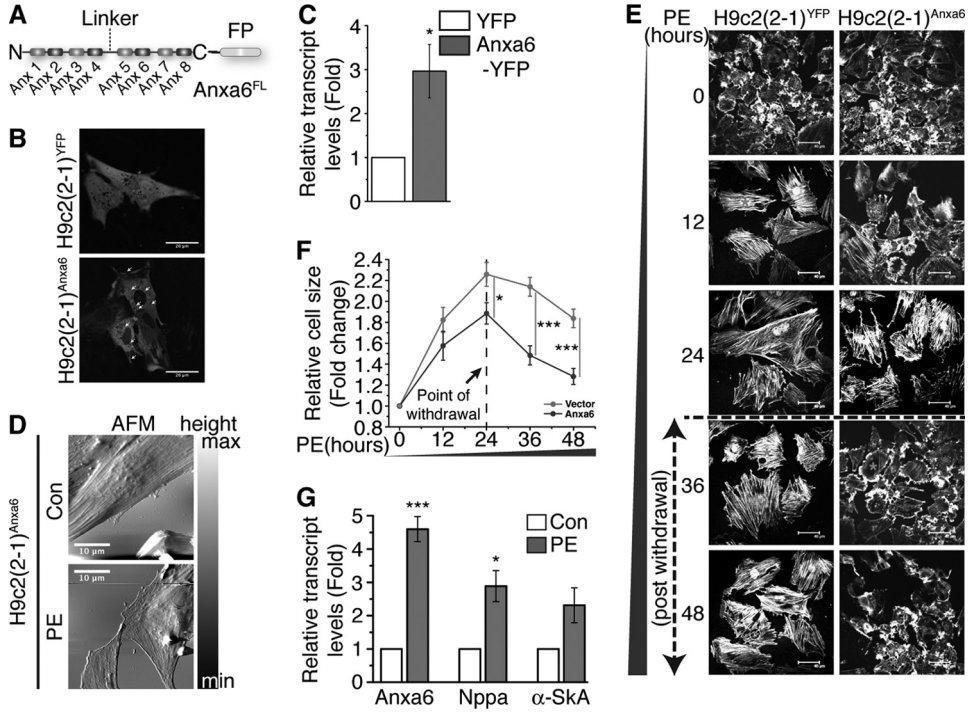

FIGURE 3. **Anxa6 protects against PE-induced hypertrophy.** H9c2 cardiomyocytes stably expressing YFP or Anxa6-YFP were analyzed for the effects of Anxa6 on hypertrophic phenotypes under PE treatment. *A*, schematic representation of a construct encoding Anxa6 tagged with fluorescent proteins (*FP*). *Anx*, annexin repeats. Here, the C-terminal tag corresponds to ZsYellow1(YFP). *B*, confocal micrographs of cells stably expressing YFP ($H9c2^{YFP}$) or Anxa6-YFP ($H9c2^{Anxa6\text{-}YFP}$). *Scale bar*, 20 μm. *Arrowheads*, signals from juxtanuclear punctate structures and plasma membrane in $H9c2^{Anxa6\text{-}YFP}$ cells. Note the reduced nuclear signal in Anxa6-expressing cells. *C*, relative levels of Anxa6 mRNA in $H9c2^{YFP}$ and $H9c2^{Anxa6\text{-}YFP}$ cells, quantified by qRT-PCR and presented as -fold change over control. Shown are means ± S.E. (*error bars*) of $n = 3$ experiments; *, $p < 0.05$. *D*, AFM images of live $H9c2^{Anxa6\text{-}YFP}$ cells, without PE (*Con*) or treated with PE for 24 h. *Scale bar*, 10 μm. The *LUT bar* corresponds to height. *E*, phalloidin-stained $H9c2^{YFP}$ and $H9c2^{Anxa6\text{-}YFP}$ cells treated with PE for the indicated time periods were analyzed by confocal microscopy. A *magenta star* denotes typical representatives of each group. *Scale bar*, 40 μm. *F*, morphometric quantification of cell surface area from *E*; $n = 50$ cells; -fold changes over $t = 0$ (***, $p < 0.0001$; *, $p < 0.05$). *Dotted line* (*E* and *F*), point of PE withdrawal. *G*, -fold changes of Anxa6, Nppa, and α-SkA mRNA in control and PE-treated $H9c2^{Anxa6\text{-}YFP}$ cells, quantified by qRT-PCR; $n = 3$; ***, $p < 0.0001$; *, $p < 0.05$.

ished association between Anxa6 and pro-ANP. Deletion of the C-terminal ($Anxa6^{\Delta C}$) tail (residues 600–673) did not have any gross effect on localization patterns but partially abrogated the association. Obligatory compartmentalization by nuclear retention of Anxa6 ($Anxa6^{NLS}$) abolished its association with pro-ANP, whereas deletion of a putative nuclear export sequence (NES; predicted by the NetNES server) partially abrogated the association ($Anxa6^{\Delta NES}$). The T356D phosphomimic of Anxa6 ($Anxa6^{T356D}$) was more similar to $Anxa6^{FL}$. To test the necessity of Anxa6-pro-ANP association for Anxa6-mediated protection, we checked the protective nature of overexpressed ANP and questioned whether the association-deficient mutants of Anxa6 alter ANP-mediated protection against PE (Fig. 6*D*). Strikingly, ANP overexpression severely restricted hypertrophic transformation of H9c2 cells. Coexpression of $Anxa6^{\Delta N1}$ or $Anxa6^{NLS}$ with ANP-EGFP significantly abrogated such protective functions of ANP, which were partially rescued by transiently transfecting the cells with $Anxa6^{FL}$ (Fig. 6*E*). To further investigate the mechanism behind such rescue operations, we measured the release of ANP by $H9c2^{ScrambshR}$ and $H9c2^{Anxa6shR}$ into the culture medium in response to PE and Iso, which are agonists of the hormonal signals known to regulate the process. For the scrambled group, in comparison with the control cells, PE- and Iso-treated cells displayed significantly higher levels of ANP release into the media. However, for the Anxa6 shRNA group, there was no significant difference in ANP release between the control and agonist-treated cells (Fig. 6*F*).

Anxa6 Is Isoform-specific and "Necessary" but Not "Sufficient" for Evoking ANP-mediated Protection against Hypertrophy—Isoform specificity has been questioned as a determinant of Anxa6 involvement in vesicular trafficking (36, 37). We found that the shorter isoform (lacking the VAAEIL residues between 525–530) of Anxa6 (Anxa6.2), although unnoticeable in control cells, expressed to a detectable limit upon PE treatment (Fig. 7*A*). To address whether association of Anxa6 with pro-ANP is an isoform-specific activity, a VAAEIL deletion mutant of the longer isoform Anxa6.1 (Figs. 6*A* and 7*A*) was generated ($Anxa6^{\Delta VAAEIL}$). Localization of $Anxa6^{\Delta VAAEIL}$ resembled that of $Anxa6^{FL}$, with more prominent puncta (Fig. 6*B*). However, mobility of such puncta (supplemental Movie 6) resembled more of retrograde traffic than anterograde, as shown for Anxa6.1 (supplemental Movies 4 and 5). $Anxa6^{\Delta VAAEIL}$ did not colocalize with pro-ANP (Fig. 7*C*) and showed partial association with pro-ANP (Fig. 6*C*) as compared with $Anxa6^{FL}$ or T356D constructs.

When H9c2 cells cotransfected with ANP-EGFP and $Anxa6^{NLS}$ were treated with PE, cellular hypertrophy was induced, accompanied by inconspicuous punctate structures in juxtanuclear cytosol that extended to the cellular periphery (Fig. 7*D*). Such structures were negligible to undetectable in corresponding control group or vector-transfected cells (Fig.

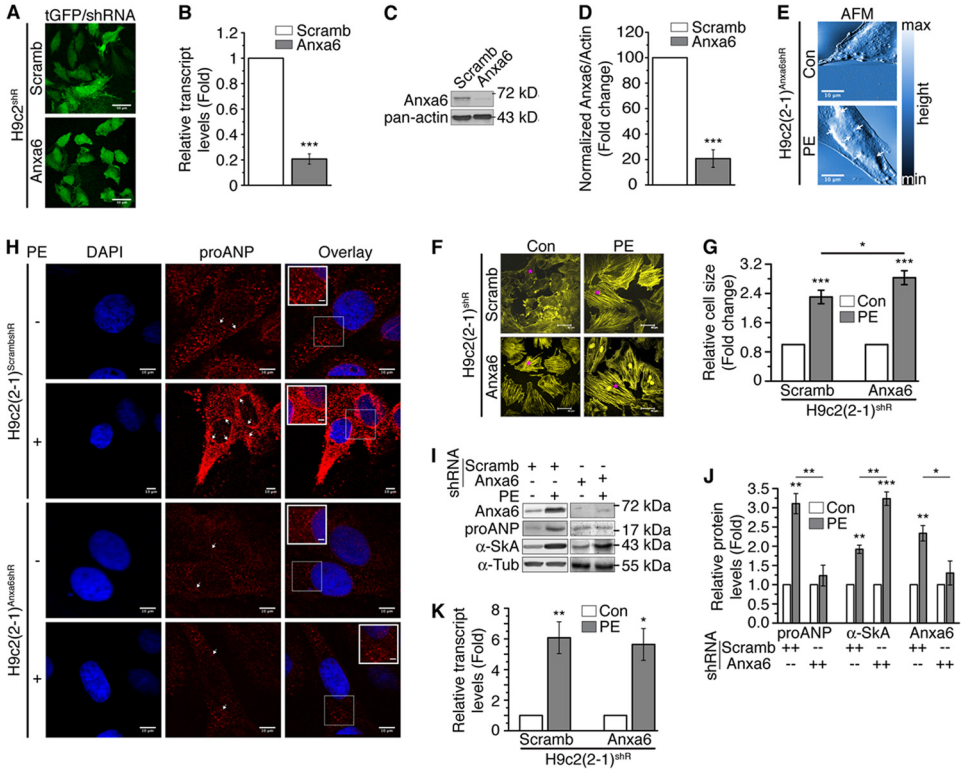

FIGURE 4. **Anxa6 knockdown augments hypertrophy but abrogates perinuclear accumulation of pro-ANP vesicles.** H9c2 cardiomyocytes stably transfected with scrambled ($H9c2^{scrambshR}$) or Anxa6 shRNA ($H9c2^{Anxa6shR}$) were analyzed for the effects of Anxa6 knockdown upon hypertrophic phenotypes induced by PE treatment for 24 h. *A*, confocal images of living H9c2 cells stably expressing tag-GFP (*tGFP*) as a marker of scramb/Anxa6 shRNA-transfected cells. *Scale bar*, 50 μm. *B*, relative levels of Anxa6 mRNA in $H9c2^{ScrambshR}$ and $H9c2^{Anxa6shR}$ cells, quantified by qRT-PCR and presented as -fold change over control. Values are means ± S.E. (*error bars*) of $n = 3$ experiments; ***, $p < 0.0001$. *C*, immunoblot showing relative protein levels of Anxa6 in scrambled ($H9c2^{ScrambshR}$) *versus* Anxa6 shRNA ($H9c2^{Anxa6shR}$)-transfected stable H9c2 cell lines. Pan-actin was used as loading control. A blot representative of average results was obtained across six passages of cells. *D*, quantification of *C*. Background-subtracted intensity values of Anxa6 were normalized with loading control. Values are means ± S.E. of $n = 3$ experiments, presented as -fold change over control; ***, $p < 0.0001$. *E*, AFM images of live $H9c2^{Anxa6shR}$ cells. *Arrowheads*, maximum height. The *LUT bar* corresponds to height. *Scale bar*, 10 μm. *F*, confocal micrographs of phalloidin-stained $H9c2^{scrambshR}$ and $H9c2^{Anxa6shR}$ cells, without PE (*Con*) or treated with PE. A *magenta star* denotes typical representatives of each group. *Scale bar*, 40 μm. *G*, -fold changes in cell size from *F*; $n = 50$ cells (***, $p < 0.0001$; *, $p < 0.05$). *H*, $H9c2^{scrambshR}$ and $H9c2^{Anxa6shR}$ cells, without PE (*Con*) or treated with PE, were immunostained for pro-ANP and analyzed by confocal microscopy. The nucleus was counterstained with DAPI. *Arrowheads*, signal intensity in the perinuclear region. *Scale bar*, 10 μm. *Insets*, magnified view of perinuclear cytosol. *Scale bar*, 2 μm. *I*, immunoblot on WCL from $H9c2^{scrambshR}$ and $H9c2^{Anxa6shR}$ cells, without PE or treated with PE, showing relative abundance of the indicated proteins. α-Tubulin was used as a loading control. *J*, densitometric quantification of *I*, showing -fold changes of the indicated proteins; $n = 3$ (***, $p < 0.0001$; **, $p < 0.01$; *, $p < 0.05$). *Plus* and *minus symbols* in *E* and *F* indicate the presence and absence of the respective components. *K*, qRT-PCR analysis of Nppa mRNA levels in $H9c2^{scrambshR}$ and $H9c2^{Anxa6shR}$ cells, without PE (*Con*) or treated with PE, expressed as -fold change over control; $n = 3$; **, $p < 0.01$; *, $p < 0.05$.

7*D*, *inset*). In the absence of Anxa6-pro-ANP association due to restricted localization of Anxa6, the appearance of such vesicular structures might be indicative of subtle pro-ANP traffic. To address whether such an occurrence represents a "leaky" phenotype of basal pro-ANP traffic, we examined involvement of factor(s), like Ca^{2+} or cholesterol, which are known to alter localization, membrane binding, and subsequently the activity of Anxa6 (38) and, in general, vesicular traffic. Pretreatment of the H9c2 cells with the Ca^{2+} ionophore ionomycin triggered enhanced membrane association of both Anxa6 and pro-ANP even without PE treatment, whereas pretreatment with the Ca^{2+} chelator BAPTA did not affect basal membrane association of Anxa6 but reduced the membrane association of Anxa6 under PE treatment (Fig. 7, *E* and *F*). In either condition, BAPTA pretreatment caused total loss of pro-ANP in the membrane fraction, suggesting that association of these two proteins is Ca^{2+}-dependent. Furthermore, pretreatment of cells with the cholesterol chelator MβCD abolished colocalization between Anxa6 and pro-ANP, even after 24 h of PE treatment (Fig. 7*G*).

To evaluate the necessity of Ca^{2+} in directing pro-ANP-SG trafficking, pro-ANP-EGFP was overexpressed in the $H9c2^{Anxa6(\Delta C)}$ cell line and treated with PE for 9 h (time point having a high anisotropy value of Anxa6). As shown (Fig. 7*H* and supplemental Movie 7), the lack of the Anxa6 C terminus affected anterograde movement of pro-ANP-SG, which was partially restored (within 2–5 min) by the addition of ionomycin. Thus, it is possible that a cholesterol-mediated recruitment of Anxa6 to pro-ANP-SG might be necessary to deliver Ca^{2+} for regulated exocytosis, which in turn, is essential for ANP-mediated regulation of hypertrophy. In other words, Anxa6 seems to be "necessary" but not "sufficient" for driving ANP-dependent counterhypertrophic signaling, which may account for the partial restoration of cell size by $Anxa6^{FL}$, as observed in Fig. 6*E*.

Dynamics of Anxa6 Facilitate Counterhypertrophic Responses in Cardiomyocytes—To ascertain further that the dynamics of Anxa6 (Fig. 5 and supplemental Movies 3–5) are involved in its counterhypertrophic function, we used the T356D phosphomimic of Anxa6, which has a more open and flexible struc-

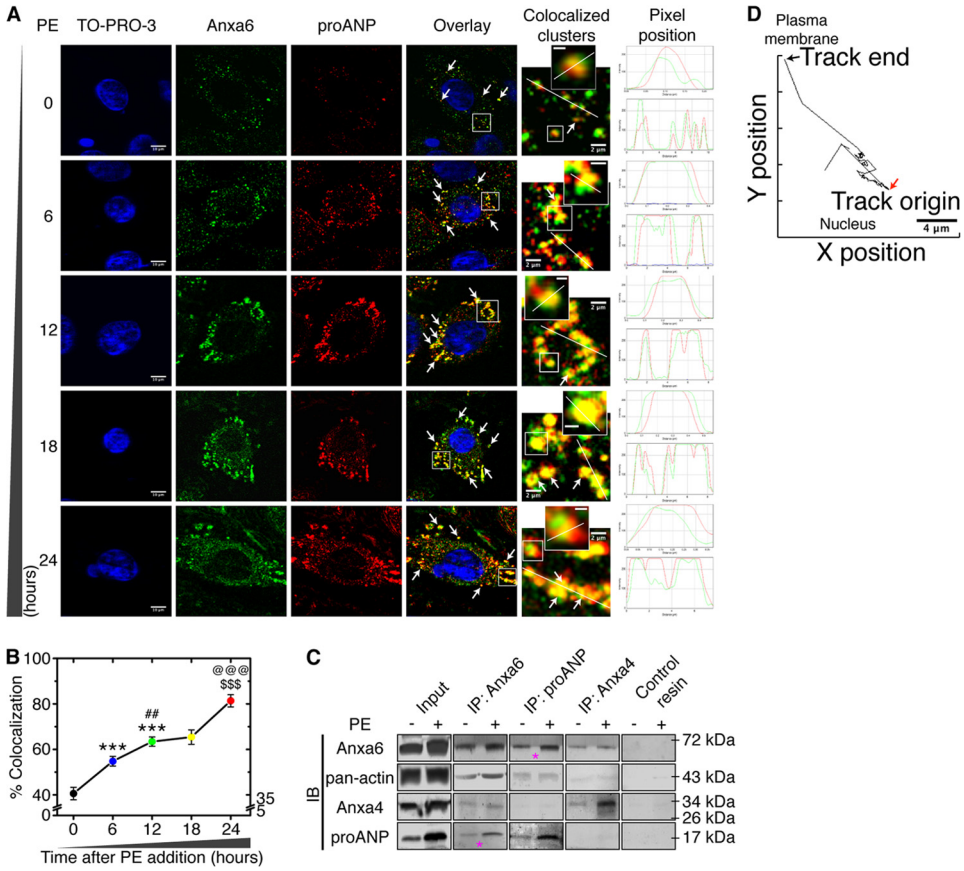

FIGURE 5. **Anxa6 progressively associates with pro-ANP in the course of PE treatment.** H9c2 cells treated with PE were examined for association between Anxa6 and pro-ANP. *A*, confocal micrographs of cells double-immunostained for Anxa6 (*pseudocolored green*) and pro-ANP (*pseudocolored red*) at the indicated time points after PE addition were analyzed for colocalization. Nuclei labeled with TO-PRO-3 (*pseudocolored blue*). *Scale bar*, 10 μm. The *colocalized cluster panel* shows a *magnified image* of the *white box* from the corresponding overlay channel. *Arrowheads*, colocalized punctate structures. *Scale bar*, 2 μm. *Inset*, magnified view of individual puncta marked by a *white box*. *Scale bar*, 0.5 μm. Line profiles corresponding to the indicated lines in the *colocalized cluster panel* and *insets* are presented in the *lower* and *upper plots*, respectively, of the *line profile panel*. *B*, degree of colocalization expressed as a percentage from Manders' overlapping coefficients (proportion of *green* overlapping *red*); $n \geq 20$ cells; ***, p (with $t = 0$) < 0.0001; $$$, p (with $t = 12 < 0.0001$); @@@, p (with $t = 18$) < 0.0001; ##, p (with $t = 6$) < 0.01. *C*, WCL (input) were subjected to IP, followed by immunoblot (*IB*) analysis of the immunoprecipitate. Antibodies used for IP are indicated at the *top*, whereas those used for immunoblot are indicated on the *left*. Control resin served as a negative control. Annexin A4 (*Anxa4*) and pan-actin were used as positive controls for IP and immunoblot, respectively. A *red star* demarcates interactions of interest. *D*, track of Anxa6-YFP cluster marked in supplemental Movie 4. *Scale bar*, 4 μm. *Error bars*, S.E.

ture that can simultaneously bind multiple membranes (39, 40). We found that membrane association of $Anxa6^{T356D}$ under PE treatment was more prominent than that of $Anxa6^{FL}$ (Fig. 8, *A* and *B*), and $H9c2^{Anxa6(T356D)}$ displayed superior protection over $H9c2^{Anxa6(FL)}$ in regulating cell surface area (Fig. 8, *C* and *D*), thus indicating a necessity of conformation-dependent dynamics for promoting counterhypertrophic activity of Anxa6.

DISCUSSION

Protein dynamics play a vital role in the regulation of fundamental biochemical processes in living cells, deregulations of which are known to be associated with a host of clinical conditions (41). Participation of Anxa6 in vesicular trafficking has been well characterized, and the protein is known to associate with endosomes and secretory vesicles (37, 42, 43). Here we show that the cytosolic 4dynamics of Anxa6 confer sustained protection against cardiomyocyte hypertrophy by associating with and regulating pro-ANP traffic, an endogenous counterhypertrophic factor (44). These conclusions are based on gain- and loss-of-function approaches involving Anxa6 in H9c2 cardiomyocytes.

With increasing needs to reduce the number of animals in laboratory research, a cardiomyocyte cell line like H9c2 provides a valuable animal origin-free alternative (21). In this regard, our data on single cell-based analysis of PE-treated H9c2 cells (Fig. 1) are comparable with changes brought about in primary cardiomyocytes exposed to hypertrophic insults *in vivo* (45). Consistent with earlier reports that Anxa6 is increased in hypertrophied and failing heart (16), it is up-regulated in hypertrophied H9c2 cardiomyocytes with a distinct punctate appearance (Fig. 2). Involvement of Anxa6 in the hypertrophic process is apparent because gain-of-function restricts the changes brought about by PE, at least partially (Fig. 3). Such findings are further confirmed by Anxa6 knockdown, which augments hypertrophic transformation of H9c2 cells, both phenotypically and biochemically (Fig. 4).

Increased expression of ANP is a well established marker of pathological cardiac hypertrophy (4). Despite the appearance of augmented hypertrophied phenotypes, the level and characteristic spatial distribution of pro-ANP were unchanged in PE-treated $H9c2^{Anxa6shR}$ cells (Fig. 4, *H–J*). It is not due to an upstream signaling failure to elevate ANP gene expression because qRT-PCR

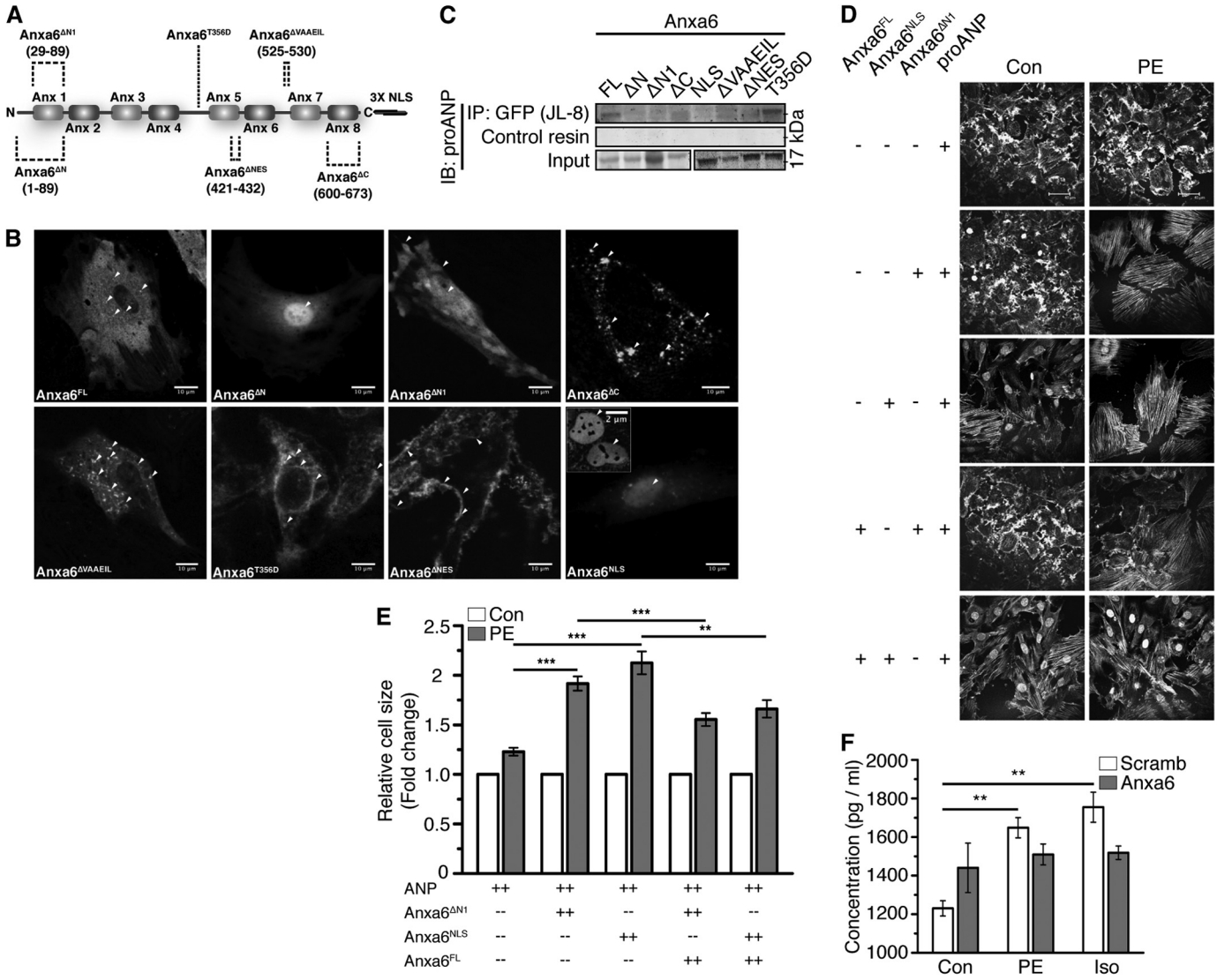

FIGURE 6. **Counterhypertrophic protection by Anxa6 is pro-ANP-dependent.** *A*, schematic map of Anxa6 mutants. The *lower segment* shows the Anxa6^{NLS} construct, with an N-terminal AcGFP1 tag. *B*, localization patterns of Anxa6 mutants described in *A*, in live H9c2 cells, compared with the wild type protein (Anxa6^{FL}). *Arrowheads*, enrichment of mutant protein levels in the indicated compartments and cytosolic punctate appearance. *Scale bar*, 10 μm. *C*, immunoblot showing co-IP of GFP with pro-ANP in WCL from cells stably expressing the indicated constructs, after 12 h of PE treatment. *D*, confocal images of phalloidin-stained cells expressing the indicated constructs, without PE (*Con*) or treated with PE for 24 h. *Scale bar*, 40 μm. A *magenta star* at the *center* of a cell denotes typical representatives of each group. *Plus* and *minus symbols* indicate the presence or absence, respectively, of the indicated constructs. *E*, quantification of cell surface area by phalloidin staining of H9c2 cells coexpressing ANP-EGFP with Anxa6$^{\Delta N1}$ or Anxa6^{NLS}, with or without Anxa6^{FL} constructs, after 24 h of PE treatment; $n = 50$ cells; ***, $p < 0.0001$; **, $p < 0.01$. *F*, ANP levels in the culture medium of scrambled and Anxa6 shRNA-expressing cells treated with PE or Iso, as compared with control. Data are expressed as means ± S.E. (*error bars*) ($n = 3$). **, $p < 0.01$ *versus* control.

reveals an up-regulated Nppa expression profile in H9c2^{Anxa6shR} cells, similar to PE-treated H9c2^{ScrambshR} cells (Fig. 4*K*). This brought into question whether Anxa6 is necessary for maintaining stability or turnover rates of pro-ANP. The absence of Anxa6 might have affected PE-induced accumulation of juxtanuclear pro-ANP-SG, a prerequisite for vesicle aggregation and regulated exocytosis of ANP (46, 47). Interestingly, several reports demonstrated that ANP exhibits local counterhypertrophic activities (23, 48, 49), and Anxa6 is an atrial SG-binding protein, a major component of which is pro-ANP (50). Therefore, we inquired whether Anxa6 associates with pro-ANP to confer its protective functions via ANP-dependent mechanisms.

A progressive association of Anxa6 with pro-ANP is evidenced, where they seem to aggregate in the course of PE treatment (Fig. 5). Intriguingly, such clustering of puncta also represents a signature pattern of regulated exocytosis (47). Localization of pro-ANP in cardiomyocytes is restricted to punctate vesicular structures (51) that follow a regulated secretory pathway rather than a constitutive one under pathological hypertrophy (44). Anxa6-pro-ANP association also appears to be dynamic, as visualized in cells co-expressing these proteins, where a real-time overlap of Anxa6 and pro-ANP is evident (supplemental Movie 3). Moreover, movement of Anxa6 clusters occurs parallel to anterograde (41) vesicular traffic (supplemental Movies 4 and 5) in the course of PE treatment. It appears that adrenergic stimulation of H9c2 cells provokes spatiotemporal dynamics of Anxa6 involving pro-ANP vesicular traffic. The functional significance of such association between Anxa6 and pro-ANP is apparent from the fact that overexpression of

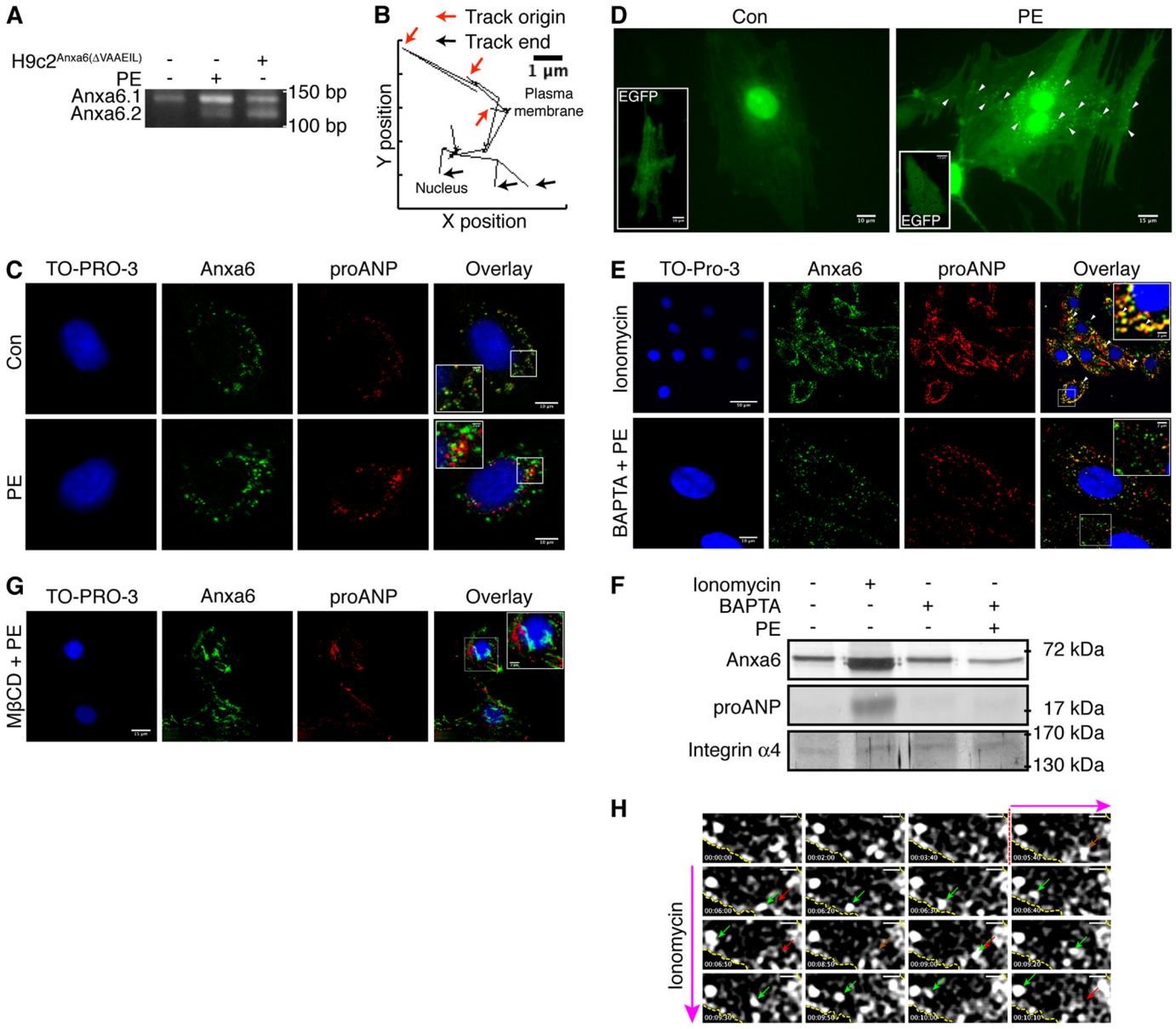

FIGURE 7. **A "necessary" but not "sufficient" mechanism of isoform-dependent Anxa6 activity drives pro-ANP traffic.** *A*, total RNA extracted from control, PE-treated, or Anxa6$^{\Delta VAAEIL}$ cells was subjected to RT-PCR using the primers indicated in Table 2, and the PCR products were analyzed in 2.5% agarose gel. The figure shows distinct amplification of either isoform of Anxa6 (Anxa6.1, 137 bp; Anxa6.2, 119 bp) in PE-treated and Anxa6$^{\Delta VAAEIL}$-overexpressing cells. The smaller isoform (Anxa6.2) was undetectable in control cells. *B*, trajectory of Anxa6$^{\Delta VAAEIL}$ clusters shown in supplemental Movie 6. *Scale bar*, 1 μm. *C*, confocal micrographs of H9c2$^{Anxa6(\Delta VAAEIL)}$ cells, double-immunostained for Anxa6 (*pseudocolored green*) and pro-ANP (*pseudocolored red*), without PE (*Con*) or treated with PE for 24 h. Nuclei were labeled with TO-PRO-3 (*pseudocolored blue*). *Scale bar*, 10 μm. *Inset*, magnified view of perinuclear cytosol marked by a *white box*. *Scale bar*, 2 μm. *D*, micrographs of H9c2 cells coexpressing Anxa6^{NLS} and ANP-EGFP, without PE (*Con*) or treated with PE for 24 h. *Arrowheads*, vesicular structures. *Scale bar*, 10 μm (*Con*) and 15 μm (*PE*). *Inset*, H9c2^{EGFP} cells of corresponding treatment groups. *Scale bar*, 10 μm. *E*, confocal micrographs of cells treated with ionomycin or with BAPTA and PE and double-immunostained for Anxa6 and pro-ANP. Nuclei were counterstained with TO-PRO-3. *Arrowheads*, overlapping clusters in the juxtanuclear cytosol. *Scale bar*, 50 μm (ionomycin) and 10 μm (BAPTA). *Inset* in *overlay*, *magnified view* of the area demarcated by the *white box*. *Scale bar*, 2 μm. *F*, immunoblot of Anxa6 and pro-ANP protein levels in membrane fractions of cells, in the absence or presence of PE for 24 h and without or pretreated with ionomycin or BAPTA, as indicated. Integrin-α4 was used as a loading control. *G*, montage of the indicated *frames* from supplemental Movie 7, showing the mobility of ANP-EGFP clusters in H9c2$^{Anxa6(\Delta C)}$ cells, before and after ionomycin addition. *Scale bar*, 2 μm. *Dotted yellow line* at the *top right* demarcates the nuclear periphery, whereas that at the *bottom left* demarcates the cellular periphery. *Orange arrowheads*, initial positions of the indicated clusters. *Green* and *red arrowheads* in *subsequent frames* indicate relative and initial positions of clusters. *H*, confocal micrographs of H9c2 cells, preincubated with 50 mM MβCD for 30 min and treated with PE for 24 h, immunostained for Anxa6 (*pseudocolored green*) and pro-ANP (*pseudocolored red*), without PE (*Con*) or treated with PE for 24 h. Nuclei were labeled with TO-PRO-3 (*pseudocolored blue*). *Scale bar*, 15 μm. *Inset*, *magnified view* of perinuclear cytosol marked by a *white box*. *Scale bar*, 2 μm.

pro-ANP offers substantial protection against PE, which is markedly abrogated when Anxa6 fails to interact with ANP due to domain deletion or forced compartmentalization. Such loss of protection is significantly rescued by Anxa6^{FL} (Fig. 6, *B–E*), suggesting that the counterhypertrophic activity of Anxa6 depends on its association with pro-ANP. Moreover, reduced levels of Anxa6 in H9c2^{Anxa6shR} cells severely abrogated PE- or Iso-induced release of ANP, showing that putative changes in pro-ANP modulated by Anxa6 translate into functionally significant differences in ANP release (Fig. 6*F*). Such activity also

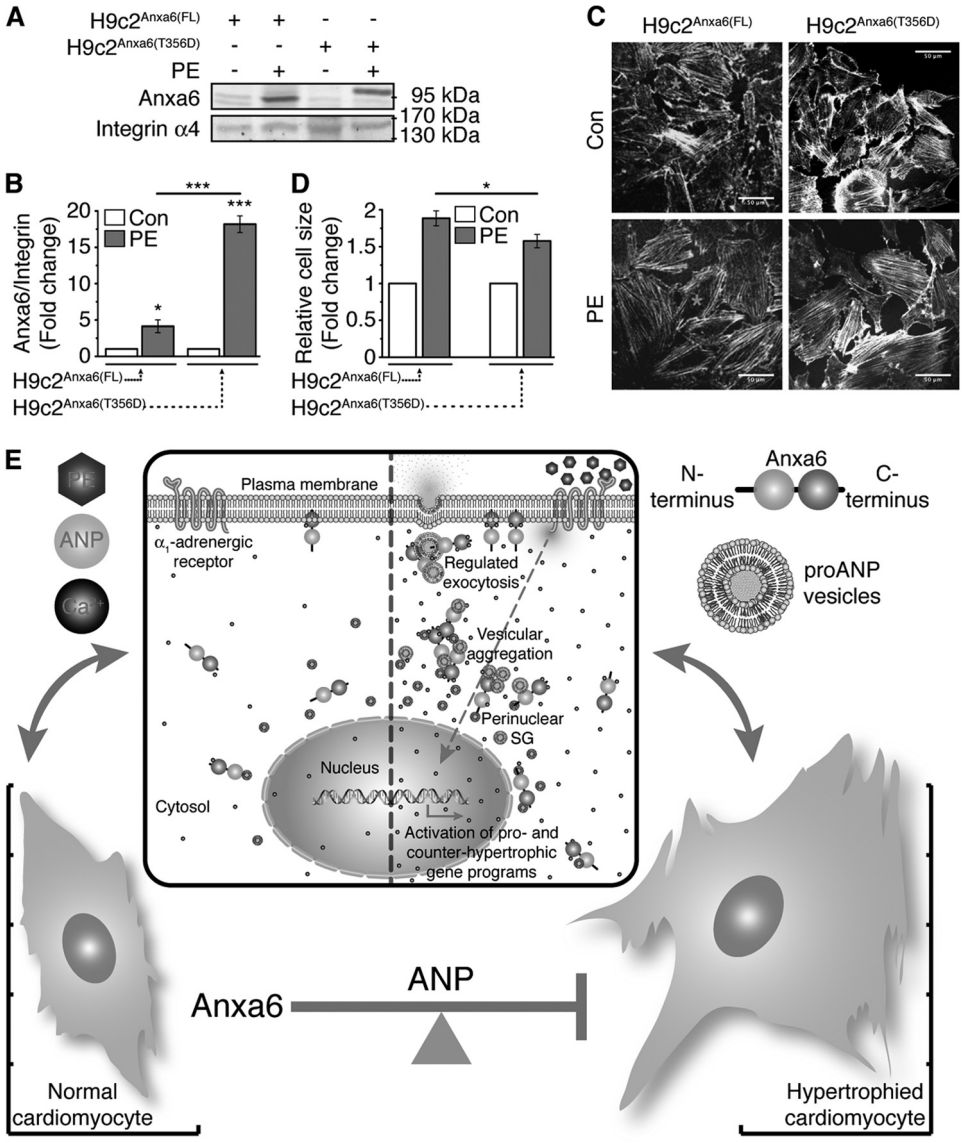

FIGURE 8. **Dynamics of Anxa6 potentiate counterhypertrophic responses in cardiomyocytes.** *A*, immunoblot showing Anxa6 protein level in membrane fractions of H9c2$^{Anxa6(FL)}$ and H9c2$^{Anxa6(T356D)}$ cells, without PE (−) or treated with PE (+) for 24 h. Integrin-α4 was used as a loading control. *B*, -fold changes in protein level of Anxa6 from A; $n = 3$; ***, $p < 0.0001$; *, $p < 0.05$. *C*, confocal micrographs of phalloidin-stained H9c2$^{Anxa6(FL)}$ and H9c2$^{Anxa6(T356D)}$ cells, without PE (−) or treated with PE (+) for 24 h. A *magenta star* denotes typical representatives of each group. *Scale bar*, 50 μm. *D*, -fold changes in cell area from C; $n =$ 50 cells (H9c2$^{Anxa6(FL)}$); $n = 40$ cells (H9c2$^{Anxa6(T356D)}$); *, $p < 0.05$. *E*, schematic depiction of Anxa6 participating in regulated vesicular traffic of pro-ANP-SG, under hypertrophic challenges like PE, in a Ca^{2+}-dependent manner that drives ANP-dependent counterhypertrophic functions. α_1-AR stimulation by PE caused elevation of cytosolic Ca^{2+} and activation of pro- and counterhypertrophic gene programs, resulting in mobilization of Anxa6 in cytosol and the appearance of pro-ANP-SG in juxtanuclear cytosol. Anxa6 associates with pro-ANP-SG in a Ca^{2+}-dependent manner to facilitate vesicle aggregation and regulated exocytosis of ANP that triggers downstream counterhypertrophic responses in cardiomyocytes. *Error bars*, S.E.

seems to be specific for the larger isoform of Anxa6 rather than the smaller one (Anxa6$^{\Delta VAAEIL}$), which displays a punctate distribution pattern but does not associate with pro-ANP or participate in anterograde trafficking (Fig. 7, *A–C*, and supplemental Movie 6). This is consistent with the finding that the structural differences between the two isoforms due to the lack of the VAAEIL residues alters their functional behavior and interaction with membranes (45). It is likely that, as also noted by others, Anxa6 isoforms interact with different targets and behave differentially in vesicular and endocytic trafficking pathways (36, 37).

A limited vesicular network of pro-ANP extending from perinuclear cytosol to the cell periphery was visualized (Fig. 7*D*) in cells coexpressing ANP-EGFP and Anxa6^{NLS}. Such inconspicuous pro-ANP-SG is insufficient to protect the cells against hypertrophic insults and may be representative of a leaky basal pro-ANP traffic. This called into question the involvement of factors other than Anxa6 in regulation of pro-ANP traffic. Ca^{2+} has long been known to be a critical packaging and driving factor for sorting of pro-ANP vesicles (47), and Anxa6 is reported to be a cytosolic Ca^{2+}-sequestering agent (18). Consistent with these, ionomycin alone is sufficient to colocalize Anxa6 with pro-ANP, with increased deposition in membrane fractions, whereas removal of Ca^{2+} by BAPTA completely abrogates the colocalization and membrane deposition, even under PE treatment (Fig. 7, *E* and *F*). Thus, a failure by

Anxa6^{NLS} to bind cytosolic Ca^{2+} may result in defective vesicular traffic of pro-ANP that can account for the loss of protection in these cells. Also, cholesterol has been described as a factor governing localization and membrane binding of Anxa6 in some cell types (34, 57, 58). Pretreatment of H9c2 cells with the cholesterol chelator MβCD abolished colocalization of Anxa6 and pro-ANP (Fig. 7*G*), suggesting that the dynamic interaction between Anxa6 and pro-ANP also depends on membrane cholesterol content. pro-ANP is known to be a major membrane-associated protein of rat atrial SG (52). Because pro-ANP-EGFP clusters are relatively immobile in H9c2$^{Anxa6(\Delta C)}$ cells, which can be partially restored by ionomycin (Fig. 7*H* and supplemental Movie 7), it is possible that Anxa6 is critical for delivering Ca^{2+} necessary for pro-ANP trafficking. It has long been known that the C terminus of Anxa6 is essential for Ca^{2+} and phospholipid binding (39). Given that the Anxa6$^{\Delta C}$ mutant exhibits partial association with pro-ANP, it is likely that Ca^{2+} binding at the C terminus induces the conformational change in the N terminus (53) necessary to associate with pro-ANP-SG, thereby driving regulated vesicular traffic of pro-ANP. Furthermore, the discovery of Ca^{2+}-binding domains in pro-ANP (25) also strengthens the idea that Anxa6 delivers Ca^{2+} to pro-ANP that may be necessary for its packaging or processing.

A functional role of Anxa6 dynamics receives further support from the stable expression of the Anxa6^{T356D} mutant, which displayed a considerably higher degree of membrane binding in hypertrophied cells (Fig. 8, *A* and *B*). This phosphomimic of Anxa6 reportedly exhibits a conformation resembling the Ca^{2+}-bound state of WT and is assumed to possess a more flexible, open structure, enabling it to interact with multiple membranes simultaneously (39, 40, 54). Furthermore, cells stably expressing T356D were found to be superior to WT Anxa6 in defending PE-induced hypertrophy (Fig. 8, *C* and *D*). This may have multiple implications; a conformation reflecting Ca^{2+}-bound Anxa6 would allow T356D to bypass the necessity of Ca^{2+} to bind membranous structures, at least partially. Moreover, the open architecture of T356D would allow Ca^{2+} to induce vesicular aggregation more efficiently than WT, thereby accelerating regulated vesicular exocytosis of pro-ANP, a prerequisite for eliciting counterhypertrophic responses by natriuretic peptides (44, 55, 56).

Therefore, our findings indicate that Anxa6 mediates counterhypertrophic signaling in cardiomyocytes by participating in the trafficking of pro-ANP (Fig. 8*E*). Because basal pro-ANP levels were unaltered in H9c2^{Anxa6shR} cells, it is possible that Anxa6 participates in the regulated rather than constitutive exocytosis of pro-ANP and participates in the formation of an ANP secretagogue under hypertrophic challenge. In this regard, earlier studies that described Anxa6 to be an inhibitor of secretion rather than a modulator, as described herein, relied on characterization of purified proteins and vesicles in competitive binding or analyzed tissue-specific distribution of the protein (9, 59). Such studies did not take into account the dynamic changes that may occur in protein function under stress at the cellular level (60). But clearly, the mechanism of Anxa6 mobilization in hypertrophied cardiomyocytes and its subsequent integration into pro-ANP transport warrant further investigation. The status of ANP signaling has not been studied in animal models of Anxa6, but knock-out mice lacking Anxa6 displayed faster calcium removal from cytosol (18). This, together with lowered Anxa6 levels in transition from hypertrophy to heart failure (16), leaves the question open about possible involvement of Anxa6 in regulation of ANP biology. However, as documented earlier (13, 14), functional redundancies within the annexin family may well compensate for the lack of altered ANP signaling at the systemic level in Anxa6 knock-out mice and should be studied at the cellular level to rule out possible interference in determining changes in ANP signaling.

In conclusion, the present study depicts a hitherto uncharacterized function of Anxa6 in maneuvering regulated traffic of pro-ANP in hypertrophied H9c2 cardiomyocytes and thereby potentiating ANP-mediated counterhypertrophic responses. In this regard, it would be interesting to determine whether Anxa6 can afford similar protective functions in genetic animal models *in vivo* or whether the counterhypertrophic potential of Anxa6 could be harnessed therapeutically. Further studies would contribute to a better understanding of cardioprotective roles played by Anxa6 in the hypertrophied arena.

Acknowledgments—We thank Professor Anna Huttenlocher (University of Wisconsin, Madison, WI) for the tol2-mpx-Dendra2 construct, Swapan Mondal for laboratory assistance, and Thangamuniyadi Muruganandan and Diptadeep Sarkar for technical support with AFM and spinning disc microscopy, respectively. A. B. gratefully acknowledges the Central Confocal and Atomic Force Microscopy Facility at IICB (funded by CSIR) and the CSIR-IICB Live Cell Imaging Facility (co-funded by the Wellcome Trust and CSIR) for the imaging experiments.

REFERENCES

1. Jorgensen, P., and Tyers, M. (2004) How cells coordinate growth and division. *Curr. Biol.* **14,** R1014–R1027
2. Dorn, G. W., 2nd, Robbins, J., and Sugden, P. H. (2003) Phenotyping hypertrophy. Eschew obfuscation. *Circ. Res.* **92,** 1171–1175
3. Frey, N., and Olson, E. N. (2003) Cardiac hypertrophy. The good, the bad, and the ugly. *Annu. Rev. Physiol.* **65,** 45–79
4. Hunter, J. J., and Chien, K. R. (1999) Signaling pathways for cardiac hypertrophy and failure. *N. Engl. J. Med.* **341,** 1276–1283
5. Camors, E., Monceau, V., and Charlemagne, D. (2005) Annexins and Ca^{2+} handling in the heart. *Cardiovasc. Res.* **65,** 793–802
6. Koese, M., Rentero, C., Kota, B. P., Hoque, M., Cairns, R., Wood, P., Vilà de Muga, S., Reverter, M., Alvarez-Guaita, A., Monastyrskaya, K., Hughes, W. E., Swarbrick, A., Tebar, F., Daly, R. J., Enrich, C., and Grewal, T. (2013) Annexin A6 is a scaffold for PKCα to promote EGFR inactivation. *Oncogene* **32,** 2858–2872
7. Monastyrskaya, K., Babiychuk, E. B., and Draeger, A. (2009) The annexins. Spatial and temporal coordination of signaling events during cellular stress. *Cell. Mol. Life Sci.* **66,** 2623–2642
8. Locate, S., Colyer, J., Gawler, D. J., and Walker, J. H. (2008) Annexin A6 at the cardiac myocyte sarcolemma. Evidence for self-association and binding to actin. *Cell Biol. Int.* **32,** 1388–1396
9. Donnelly, S. R., and Moss, S. E. (1997) Annexins in the secretory pathway. *Cell. Mol. Life Sci.* **53,** 533–538
10. Hazarika, P., Kaetzel, M. A., Sheldon, A., Karin, N. J., Fleischer, S., Nelson, T. E., and Dedman, J. R. (1991) Annexin VI is associated with calcium-sequestering organelles. *J. Cell. Biochem.* **46,** 78–85
11. Jäckle, S., Beisiegel, U., Rinninger, F., Buck, F., Grigoleit, A., Block, A., Gröger, I., Greten, H., and Windler, E. (1994) Annexin VI, a marker protein of hepatocytic endosomes. *J. Biol. Chem.* **269,** 1026–1032

12. Raynal, P., and Pollard, H. B. (1994) Annexins. The problem of assessing the biological role for a gene family of multifunctional calcium- and phospholipid-binding proteins. *Biochim. Biophys. Acta* **1197,** 63–93
13. Hawkins, T. E., Roes, J., Rees, D., Monkhouse, J., and Moss, S. E. (1999) Immunological development and cardiovascular function are normal in annexin VI null mutant mice. *Mol. Cell. Biol.* **19,** 8028–8032
14. Chlystun, M., Campanella, M., Law, A. L., Duchen, M. R., Fatimathas, L., Levine, T. P., Gerke, V., and Moss, S. E. (2013) Regulation of mitochondrial morphogenesis by annexin a6. *PloS One* **8,** e53774
15. Song, G., Campos, B., Wagoner, L. E., Dedman, J. R., and Walsh, R. A. (1998) Altered cardiac annexin mRNA and protein levels in the left ventricle of patients with end-stage heart failure. *J. Mol. Cell Cardiol.* **30,** 443–451
16. Trouvé, P., Legot, S., Bélikova, I., Marotte, F., Bénévolensky, D., Russo-Marie, F., Samuel, J. L., and Charlemagne, D. (1999) Localization and quantitation of cardiac annexins II, V, and VI in hypertensive guinea pigs. *Am. J. Physiol.* **276,** H1159–H1166
17. Mishra, S., Chander, V., Banerjee, P., Oh, J. G., Lifirsu, E., Park, W. J., Kim do, H., and Bandyopadhyay, A. (2011) Interaction of annexin A6 with α actinin in cardiomyocytes. *BMC Cell Biol.* **12,** 7
18. Song, G., Harding, S. E., Duchen, M. R., Tunwell, R., O'Gara, P., Hawkins, T. E., and Moss, S. E. (2002) Altered mechanical properties and intracellular calcium signaling in cardiomyocytes from annexin 6 null-mutant mice. *FASEB J.* **16,** 622–624
19. Hescheler, J., Meyer, R., Plant, S., Krautwurst, D., Rosenthal, W., and Schultz, G. (1991) Morphological, biochemical, and electrophysiological characterization of a clonal cell (H9c2) line from rat heart. *Circ. Res.* **69,** 1476–1486
20. Alkistis Frentzou, G., Collier, M. E., Seymour, A. M., and Ettelaie, C. (2010) Differential induction of cellular proliferation, hypertrophy and apoptosis in H9c2 cardiomyocytes by exogenous tissue factor. *Mol. Cell. Biochem.* **345,** 119–130
21. Watkins, S. J., Borthwick, G. M., and Arthur, H. M. (2011) The H9C2 cell line and primary neonatal cardiomyocyte cells show similar hypertrophic responses *in vitro*. *In Vitro Cell. Dev. Biol. Anim.* **47,** 125–131
22. Mann, D. L., and Bristow, M. R. (2005) Mechanisms and models in heart failure. The biomechanical model and beyond. *Circulation* **111,** 2837–2849
23. Molkentin, J. D. (2003) A friend within the heart. Natriuretic peptide receptor signaling. *J. Clin. Invest.* **111,** 1275–1277
24. Yoo, S. K., and Huttenlocher, A. (2011) Spatiotemporal photolabeling of neutrophil trafficking during inflammation in live zebrafish. *J. Leukoc. Biol.* **89,** 661–667
25. Baertschi, A. J., Monnier, D., Schmidt, U., Levitan, E. S., Fakan, S., and Roatti, A. (2001) Acid prohormone sequence determines size, shape, and docking of secretory vesicles in atrial myocytes. *Circ. Res.* **89,** E23–E29
26. Planavila, A., Laguna, J. C., and Vázquez-Carrera, M. (2005) Nuclear factor-κB activation leads to down-regulation of fatty acid oxidation during cardiac hypertrophy. *J. Biol. Chem.* **280,** 17464–17471
27. Chen, M. Z., Bu, Q. T., Pang, S. C., Li, F. L., Sun, M. N., Chu, E. F., and Li, H. (2012) Tetrodotoxin attenuates isoproterenol-induced hypertrophy in H9c2 rat cardiac myocytes. *Mol. Cell. Biochem.* **371,** 77–88
28. De, K., Ghosh, G., Datta, M., Konar, A., Bandyopadhyay, J., Bandyopadhyay, D., Bhattacharya, S., and Bandyopadhyay, A. (2004) Analysis of differentially expressed genes in hyperthyroid-induced hypertrophied heart by cDNA microarray. *J. Endocrinol.* **182,** 303–314
29. Schmittgen, T. D., and Livak, K. J. (2008) Analyzing real-time PCR data by the comparative *C*(*T*) method. *Nat. Prot.* **3,** 1101–1108
30. Chudakov, D. M., Lukyanov, S., and Lukyanov, K. A. (2007) Using photoactivatable fluorescent protein Dendra2 to track protein movement. *BioTechniques* **42,** 553
31. Bolte, S., and Cordelières, F. P. (2006) A guided tour into subcellular colocalization analysis in light microscopy. *J. Microsc.* **224,** 213–232
32. Meijering, E., Dzyubachyk, O., and Smal, I. (2012) Methods for cell and particle tracking. *Methods Enzymol.* **504,** 183–200
33. Ma, H., Kien, F., Manière, M., Zhang, Y., Lagarde, N., Tse, K. S., Poon, L. L., and Nal, B. (2012) Human annexin A6 interacts with influenza a virus protein M2 and negatively modulates infection. *J. Virol.* **86,** 1789–1801
34. Sztolsztener, M. E., Strzelecka-Kiliszek, A., Pikula, S., Tylki-Szymanska, A., and Bandorowicz-Pikula, J. (2010) Cholesterol as a factor regulating intracellular localization of annexin A6 in Niemann-Pick type C human skin fibroblasts. *Arch. Biochem. Biophys.* **493,** 221–233
35. Gunteski-Hamblin, A. M., Song, G., Walsh, R. A., Frenzke, M., Boivin, G. P., Dorn, G. W., 2nd, Kaetzel, M. A., Horseman, N. D., and Dedman, J. R. (1996) Annexin VI overexpression targeted to heart alters cardiomyocyte function in transgenic mice. *Am. J. Physiol.* **270,** H1091–H1100
36. Kaetzel, M. A., Pula, G., Campos, B., Uhrin, P., Horseman, N., and Dedman, J. R. (1994) Annexin VI isoforms are differentially expressed in mammalian tissues. *Biochim. Biophys. Acta* **1223,** 368–374
37. Podszywalow-Bartnicka, P., Kosiorek, M., Piwocka, K., Sikora, E., Zablocki, K., and Pikula, S. (2010) Role of annexin A6 isoforms in catecholamine secretion by PC12 cells. Distinct influence on calcium response. *J. Cell. Biochem.* **111,** 168–178
38. Enrich, C., Rentero, C., de Muga, S. V., Reverter, M., Mulay, V., Wood, P., Koese, M., and Grewal, T. (2011) Annexin A6-linking Ca^{2+} signaling with cholesterol transport. *Biochim. Biophys. Acta* **1813,** 935–947
39. Creutz, C. E., and Snyder, S. L. (2005) Interactions of annexins with the μ subunits of the clathrin assembly proteins. *Biochemistry* **44,** 13795–13806
40. Freye-Minks, C., Kretsinger, R. H., and Creutz, C. E. (2003) Structural and dynamic changes in human annexin VI induced by a phosphorylation-mimicking mutation, T356D. *Biochemistry* **42,** 620–630
41. Brandizzi, F., and Barlowe, C. (2013) Organization of the ER-Golgi interface for membrane traffic control. *Nat. Rev. Mol. Cell Biol.* **14,** 382–392
42. Goldberg, M., Feinberg, J., Lecolle, S., Kaetzel, M. A., Rainteau, D., Lessard, J. L., Dedman, J. R., and Weinman, S. (1991) Co-distribution of annexin VI and actin in secretory ameloblasts and odontoblasts of rat incisor. *Cell Tissue Res.* **263,** 81–89
43. Grewal, T., Heeren, J., Mewawala, D., Schnitgerhans, T., Wendt, D., Salomon, G., Enrich, C., Beisiegel, U., and Jäckle, S. (2000) Annexin VI stimulates endocytosis and is involved in the trafficking of low density lipoprotein to the prelysosomal compartment. *J. Biol. Chem.* **275,** 33806–33813
44. Klaiber, M., Kruse, M., Völker, K., Schröter, J., Feil, R., Freichel, M., Gerling, A., Feil, S., Dietrich, A., Londoño, J. E., Baba, H. A., Abramowitz, J., Birnbaumer, L., Penninger, J. M., Pongs, O., and Kuhn, M. (2010) Novel insights into the mechanisms mediating the local antihypertrophic effects of cardiac atrial natriuretic peptide. Role of cGMP-dependent protein kinase and RGS2. *Basic Res. Cardiol.* **105,** 583–595
45. Sundaresan, N. R., Vasudevan, P., Zhong, L., Kim, G., Samant, S., Parekh, V., Pillai, V. B., Ravindra, P. V., Gupta, M., Jeevanandam, V., Cunningham, J. M., Deng, C. X., Lombard, D. B., Mostoslavsky, R., and Gupta, M. P. (2012) The sirtuin SIRT6 blocks IGF-Akt signaling and development of cardiac hypertrophy by targeting c-Jun. *Nat. Med.* **18,** 1643–1650
46. Masedunskas, A., Porat-Shliom, N., and Weigert, R. (2012) Regulated exocytosis. Novel insights from intravital microscopy. *Traffic* **13,** 627–634
47. Thibault, G., and Doubell, A. F. (1992) Binding and aggregation of pro-atrial natriuretic factor by calcium. *Am. J. Physiol.* **262,** C907–C915
48. Bubikat, A., De Windt, L. J., Zetsche, B., Fabritz, L., Sickler, H., Eckardt, D., Gödecke, A., Baba, H. A., and Kuhn, M. (2005) Local atrial natriuretic peptide signaling prevents hypertensive cardiac hypertrophy in endothelial nitric-oxide synthase-deficient mice. *J. Biol. Chem.* **280,** 21594–21599
49. Rosenkranz, A. C., Woods, R. L., Dusting, G. J., and Ritchie, R. H. (2003) Antihypertrophic actions of the natriuretic peptides in adult rat cardiomyocytes. Importance of cyclic GMP. *Cardiovasc. Res.* **57,** 515–522
50. Doubell, A. F., Bester, A. J., and Thibault, G. (1991) Annexins V and VI. Major calcium-dependent atrial secretory granule-binding proteins. *Hypertension* **18,** 648–656
51. Canaff, L., Brechler, V., Reudelhuber, T. L., and Thibault, G. (1996) Secretory granule targeting of atrial natriuretic peptide correlates with its calcium-mediated aggregation. *Proc. Natl. Acad. Sci. U.S.A.* **93,** 9483–9487
52. O'Donnell, P. J., Driscoll, W. J., Bäck, N., Muth, E., and Mueller, G. P. (2003) Peptidylglycine-α-amidating monooxygenase and pro-atrial natriuretic peptide constitute the major membrane-associated proteins of rat atrial secretory granules. *J. Mol. Cell Cardiol.* **35,** 915–922
53. Rescher, U., and Gerke, V. (2004) Annexins. Unique membrane binding proteins with diverse functions. *J. Cell Sci.* **117,** 2631–2639
54. Gerke, V., Creutz, C. E., and Moss, S. E. (2005) Annexins. Linking Ca^{2+} signalling to membrane dynamics. *Nat. Rev. Mol. Cell Biol.* **6,** 449–461

55. Calvieri, C., Rubattu, S., and Volpe, M. (2012) Molecular mechanisms underlying cardiac antihypertrophic and antifibrotic effects of natriuretic peptides. *J. Mol. Med.* **90,** 5–13
56. Rybkin, I. I., Kim, M. S., Bezprozvannaya, S., Qi, X., Richardson, J. A., Plato, C. F., Hill, J. A., Bassel-Duby, R., and Olson, E. N. (2007) Regulation of atrial natriuretic peptide secretion by a novel Ras-like protein. *J. Cell Biol.* **179,** 527–537
57. Ayala-Sanmartin, J. (2001) Cholesterol enhances phospholipid binding and aggregation of annexins by their core domain. *Biochem. Biophys. Res. Commun.* **283,** 72–79
58. de Diego, I., Schwartz, F., Siegfried, H., Dauterstedt, P., Heeren, J., Beisiegel, U., Enrich, C., and Grewal, T. (2002) Cholesterol modulates the membrane binding and intracellular distribution of annexin 6. *J. Biol. Chem.* **277,** 32187–32194
59. Creutz, C. E., Moss, S., Edwardson, J. M., Hide, I., and Gomperts, B. (1992) Differential recognition of secretory vesicles by annexins. European Molecular Biology Organization Course "Advanced Techniques for Studying Secretion". *Biochem. Biophys. Res. Commun.* **184,** 347–352
60. Roostalu, U., and Strähle, U. (2012) *In vivo* imaging of molecular interactions at damaged sarcolemma. *Dev. Cell* **22,** 515–529